The Influence of Convection Initiation Strength on Subsequent Simulated Supercell Evolution

MATTHEW D. FLOURNOY[a,b] AND ERIK N. RASMUSSEN[b]

[a] *Cooperative Institute for Severe and High-Impact Weather Research and Operations, University of Oklahoma, Norman, Oklahoma*
[b] *NOAA/OAR National Severe Storms Laboratory, Norman, Oklahoma*

(Manuscript received 9 March 2022, in final form 24 May 2023, accepted 26 May 2023)

ABSTRACT: Recent studies have shown how very small differences in the background environment of a supercell can yield different outcomes, particularly in terms of tornado production. In this study, we use a novel convection initiation technique to simulate six supercells with a focus on their early development. Each experiment is identical, except for the strength of thermal forcing for the initial convection initiation. Each experiment yields a mature supercell, but differences in storm-scale characteristics like updraft speed, cold pool temperature deficit, and vertical vorticity development abound. Of these, the time when the midlevel updraft strengthens is most strongly related to initiation strength, with stronger thermal forcing favoring quicker updraft development. The same is true for the low-level updraft, with the additional relationship that stronger thermal forcing also tends to yield stronger low-level updrafts for around the first 2 h of the simulations. The experiments with faster updraft development tend to be associated with more rapid surface vortex intensification; however, cold pool evolution differs between simulations with weaker versus stronger thermal forcing. Stronger thermal forcing also yields deviant rightward storm motion earlier in the supercell's life cycle that remains more consistent for the duration of the simulation. These results highlight the range of supercellular outcomes that are possible across a background environment due to differences in storm-scale initiation strength. They are also of potential importance for predicting the paths and tornado potential of supercells in real time.

SIGNIFICANCE STATEMENT: Despite a better understanding of processes related to tornado production in supercell thunderstorms, forecasters still have difficulty discriminating between tornadic and nontornadic supercells in close proximity to each other within the same severe weather event. In this study, we use six simulations of supercells to examine how these different outcomes can occur. Our results show that, given the same background environment, a storm that is more strongly initiated will exhibit faster updraft development and, possibly, quicker tornado production. The opposite can be said for storms that are more weakly initiated. Differences in initiation strength are also associated with different storm motions. These findings inspire future work to better relate supercell evolution to characteristics of initiation and the environment.

KEYWORDS: Dynamics; Storm environments; Supercells; Convective storms

1. Introduction and motivation

Several studies have explored relationships between supercells, their hazards, and their environments (e.g., Rasmussen and Blanchard 1998; Thompson et al. 2003; Craven and Brooks 2004; Coniglio and Parker 2020). These findings help forecasters, researchers, and others discriminate between environments that are generally supportive of supercells and those that are not. They do not, however, give as much insight into relationships between environmental characteristics and supercell evolutionary traits (e.g., the time between convection initiation and the right turn, low-level mesocyclone development, tornado formation). To our knowledge, only a few studies have examined time-dependent characteristics of early supercell evolution. Bluestein and Parker (1993) examined a multiyear radar climatology of convection initiation (CI) and formation along Great Plains drylines and found that the time between initiation and onset of severe hazards (deduced from verified *Storm Data* reports) was typically around 2 h. Flournoy et al. (2021) analyzed a database of field-campaign soundings and supercell paths (Coniglio and Parker 2020) and did not find any significant relationships between environmental parameters and supercell evolutionary characteristics like the time of the right turn or tornadogenesis. Using highly idealized simulations, Fischer and Dahl (2020) noted an inverse relationship between heat sink and source strengths and the time that had elapsed prior to initial surface vortex development.

We think it is likely that, in addition to the background environment, the characteristics of CI will also influence early supercell evolution. Understanding CI has been a focus of many field campaigns, perhaps most notably the International

Supplemental information related to this paper is available at the Journals Online website: https://doi.org/10.1175/MWR-D-22-0069.s1.

Flournoy's current affiliations: NOAA/NWS/NCEP Storm Prediction Center, School of Meteorology, and Cooperative Institute for Severe and High-Impact Weather Research and Operations, University of Oklahoma, Norman, Oklahoma.

Corresponding author: Matthew D. Flournoy, matthew.flournoy@noaa.gov

DOI: 10.1175/MWR-D-22-0069.1

H_2O Project (IHOP_2002; Weckwerth and Parsons 2006) and Plains Elevated Convection at Night (PECAN; Geerts et al. 2017). Many of these campaigns and associated studies have naturally focused on discriminating between characteristics of successful versus failed CI. These processes occur on a variety of scales, ranging from the background synoptic-scale environment to meso-γ-scale three-dimensional inhomogeneities (e.g., Ziegler et al. 2007; Buban et al. 2012). On smaller scales, inhomogeneities like gust fronts, horizontal convective rolls, gravity waves, and geographic effects can all influence CI (e.g., Wallace 1975; Wilson and Schreiber 1986; Carbone et al. 2002; Jorgensen and Weckwerth 2003; Trier et al. 2004). Furthermore, successful initiation is generally more likely when interactions between these features occur, leading to locally enhanced vertical velocities (e.g., Droegemeier and Wilhelmson 1985; Mahoney 1988; Carbone et al. 1990; Intrieri et al. 1990). Lock and Houston (2014) investigated a 2-yr climatology of observed successful and failed CI events and found that the most common discriminator was related to the strength of lift present in the background environment (both aloft and at the surface). Nelson et al. (2021) examined radiosonde observations of successful and failed CI events during the Remote Sensing of Electrification, Lightning, and Mesoscale/Microscale Processes with Adaptive Ground Observations–Clouds, Aerosols, and Complex Terrain Interactions (RELAMPAGO-CACTI) field campaign and found that the failure events generally contained more convective inhibition (CIN) and smaller vertical moisture gradients. They theorized that a main characteristic of the successful initiation environments was the gradual erosion of convective inhibition over time. Markowski et al. (2006) analyzed failed CI during IHOP_2002 and found that the failure was due to insufficiently strong boundary layer circulations and vertically tilted updrafts; on the other hand, cumulus clouds developing along an outflow boundary exhibited much larger vertical depths (although peak vertical velocities were similar) due to a locally enhanced mesoscale circulation.

The philosophy of this study is similar to that of Markowski (2020) in our attempts to simulate a range of supercell outcomes in identical background environments. His study featured a 25-member ensemble of high-resolution tornadic supercell simulations to address the following question: What is the intrinsic predictability of tornadic supercell thunderstorms? In his words, "it depends." Interestingly, he showed that the maximum intensities of simulated tornadoes changed when small random temperature perturbations were added to the prestorm environment. Discouragingly, it was unclear how the storms interacted with the small perturbations to yield an evolutionary path either favorable or unfavorable for strong vortex production. Furthermore, differences in storm-scale characteristics were negligible between supercells that were about to produce significant vortices and those that were not. We follow a similar motivation and technique in this study, except we introduce small systematic variations into the initiating warm tendency rather than small random variations into the background temperature field.

The respective influences of the background environment and CI processes on early supercell evolution are not independent. However, based on the aforementioned studies and the fact that both failed and successful CIs typically coexist during convective events, we believe it is useful to explore a range of initiation strengths. To do so, we simulate six supercells in identical environments that differ only in terms of the strength of their initiation. Naylor and Gilmore (2012) showed similar results when they introduced their updraft nudging initiation method, specifically that longer nudging time scales eventually yielded much larger vertical velocities (their Fig. 3b). While it was not discussed, we are fascinated by these findings and the idea that, perhaps, the variety of possible supercell evolutionary paths may be partially anticipated by differences in the strength of thermal forcing for CI. In this study, we focus on these differences and attribute them to small variations in the tendency nudging technique used to initiate convection. In doing so, we 1) shed light on storm-scale processes that are linked to characteristics of initiation and 2) posit that better understanding and observing CI might lead to real-time forecast benefit on the watch-to-warning time scale.

2. Modeling techniques

a. Model setup

We used Cloud Model 1 (CM1; Bryan et al. 2003), version 18.3, to produce our simulations. For consistency, the model is configured very similarly to recent experiments in similar environments (Coffer et al. 2017; Coffer and Parker 2017, 2018; Flournoy et al. 2020). The domain is $200 \times 200 \times 18.16$ km^3 with stretched horizontal and vertical grids. One hundred fifteen vertical levels are spaced every 20 m in the lowest 300 m AGL and stretched to every 280 m at the model top. The lowest scalar level is 10 m AGL. The horizontal grid spacing is 250 m in the central 100 km × 100 km portion of the domain and stretches to 6 km at the edges. We chose a slightly coarser grid spacing than the aforementioned studies (i.e., $dx = 125$ m) to reduce the computing time needed to run several members. Each simulation is run for 4 h with an adaptive time step, and output is written every 5 min.

We used the composite near-field tornadic VORTEX2 profile (Parker 2014) to represent the base-state environment (Fig. 1). Consistent with observations, this environment is very supportive of tornadic supercell formation in idealized simulations (e.g., Coffer et al. 2017; Flournoy et al. 2020). We used a semislip bottom boundary condition with a constant drag coefficient of 0.0014 (e.g., Coffer and Parker 2017; Flournoy et al. 2020) for all simulations. Introducing surface friction complicates the force balance given our horizontally homogenous pressure and temperature fields, which do not contain the large-scale pressure-gradient forces that offset friction in the real world. Some methods to maintain a mostly steady wind profile include applying the Coriolis force only to the perturbation winds after arriving at a balanced antitriptic state (Roberts et al. 2016) or subtracting the time tendency of horizontal momentum at each time step (Dawson et al. 2019; Roberts et al. 2020). In this study, we use the former technique and obtain a mostly steady wind profile after integrating a convection-free simulation for 8 h with surface friction (Fig. 1). This method assumes that the base-state wind profile is geostrophic, and the Coriolis force applied only to perturbation winds opposes frictional effects once a new

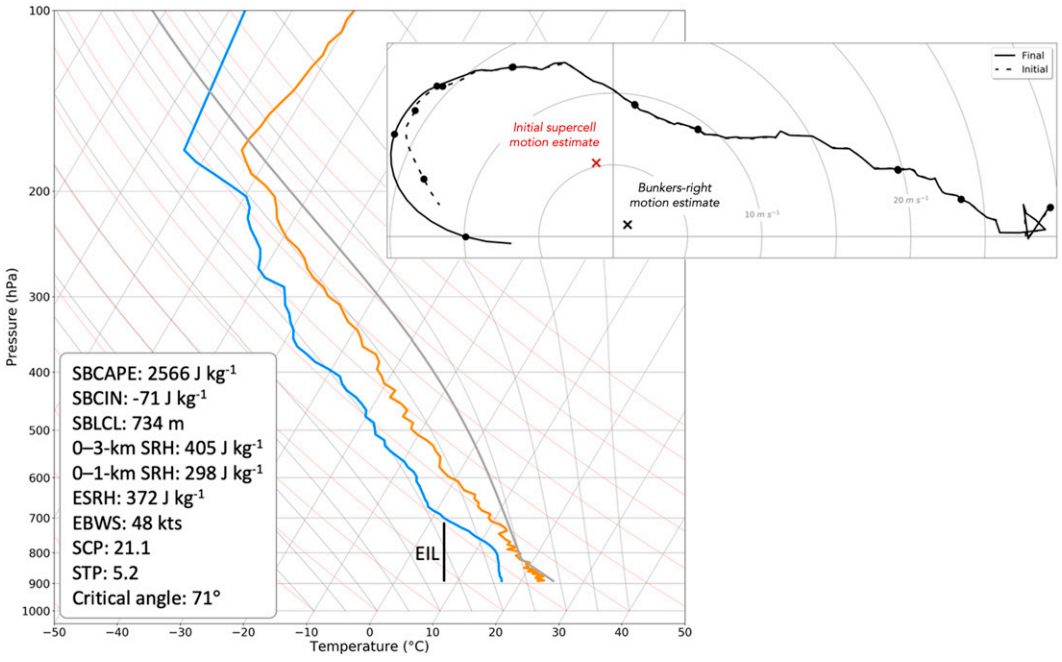

FIG. 1. The base-state (t = 0 min) environmental temperature (°C; orange), dewpoint (°C; blue), and wind (m s^{-1}; black) profiles used for all simulations. The lifted surface parcel trace and effective inflow layer (EIL) are shown. The thermodynamic profile is the composite near-field tornadic VORTEX2 profile (Parker 2014) used in some prior studies (e.g., Coffer and Parker 2017; Flournoy et al. 2020). The composite near-field tornadic VORTEX2 wind profile is dashed, and the wind profile used in this study is solid (see the text for details). Some typical parameters for the environment used in this study (e.g., the "final" hodograph) are given, including surface-based convective available potential energy (SBCAPE), surface-based convective inhibition (SBCIN), surface-based lifted condensation level (LCL), storm-relative helicity (SRH) in different layers including the effective layer (ESRH), effective bulk wind shear (EBWS), the supercell composite parameter (SCP), the significant tornado parameter (STP), and the critical angle. Black dots indicate the wind at 50, 250, 500, 1000, 2000, 3000, 6000, 8000, and 12 000 m AGL. Estimates of the initial and postturn cell motions, derived from Flournoy et al. (2021) and Bunkers et al. (2000), are marked by the red X and black X, respectively.

quasi-steady state is reached (e.g., Coffer and Parker 2017). We use the resulting wind profile as the horizontally homogeneous base state for our simulations that include the same force balance, yielding a mostly (but not perfectly) steady base-state wind profile (i.e., unperturbed by convection). Such attempts to maintain a steady horizontally uniform wind profile—characterized by veering vertical wind shear—in the presence of surface friction violate the Taylor–Proudman theorem (i.e., thermal wind balance) and introduce unphysical forces that may strongly influence near-surface vorticity budgets (Davies-Jones 2021). In this case, we believe that this problem does not influence the importance of our findings, given our focus on storm-scale evolution rather than vortex-scale vorticity budgets as well as our emphasis on more gradual CI that resembles observed supercell evolutionary time scales (as will be shown below).

b. *Varying CI strength*

To initiate discrete supercells and focus on their entire evolution (including the early stages), we use a novel CI technique that we refer to as "tendency nudging." This method introduces a time dependency (or "nudging") to the heating tendency technique introduced in Markowski and Richardson (2014). Ultimately, this adds a slowly increasing volumetric Gaussian tendency to the potential temperature field in an effort to not "shock the system" at t = 0 min. This is similar to the CI framework of Lasher-Trapp et al. (2021), who used a time-varying surface-based heat flux to gradually enable the development of thermals and, eventually, thunderstorm updrafts. Our method is not necessarily more "realistic" than other initiation schemes (e.g., especially the warm bubble, updraft nudging, forced convergence), but it does more successfully capture observed supercell evolutionary time scales by mitigating premature surface tornado-like vortices (TLVs) that may unphysically influence subsequent supercell evolution. A brief discussion of these premature TLVs, as well as the motivation for creating and using this method and its formulation and implementation in CM1, is included in the appendix.

In each experiment, the tendency nudging is centered at 3.5 km AGL and (x, y) = (−10.0 km, −20.0 km) to allow the storm to move toward the center of the domain before reaching a quasi-steady motion near 0 m s^{-1} there. Figure 2 shows the time series of the maximum heating tendency at 3.5 km AGL for the six experiments that we focus on in the next section. In all cases, the tendency nudging starts at 0 K s^{-1} at t = 0 min, reaches a maximum at t = 60 min, and decreases

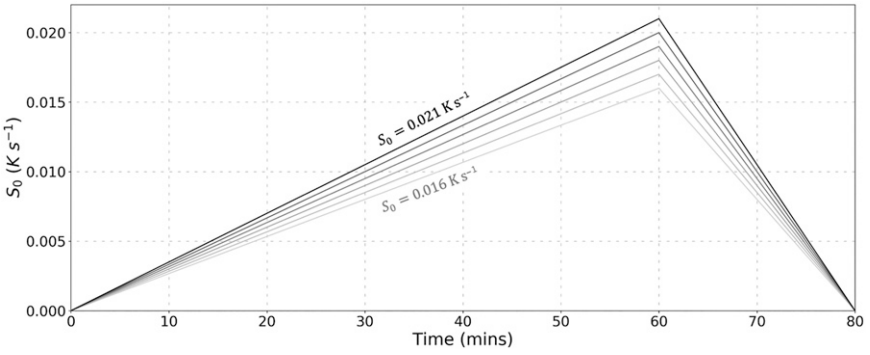

FIG. 2. Time series of the maximum heating tendencies at 3.5 km AGL for the six simulations in this study. The tendencies are all 0 K s^{-1} after t = 80 min. The S_0 = 0.016 and 0.021 K s^{-1} time series are labeled.

back to 0 K s^{-1} by t = 80 min. The nudging is applied in a volumetric area with horizontal and vertical radii of 5 and 1.5 km, respectively (see the appendix). These radii are similar to those of the heating tendencies and warm bubbles used in prior studies and yield a bottom buoyancy bound of 2 km AGL near the environmental level of free convection (1855 m; Fig. 1). The only difference between each experiment is the magnitude of the maximum tendency (S_0), which ranges from 0.016 to 0.021 K s^{-1}. The range of 0.016–0.021 K s^{-1} spans much smaller magnitudes than those used in similar studies (e.g., 0.06–0.12 K s^{-1}; Markowski and Richardson 2014; Fischer and Dahl 2020). In an effort to simulate more realistic supercell structures, we use a microphysics scheme (NSSL two moment; Mansell 2010; Mansell et al. 2010) in addition to the tendency nudging technique. As a result, unlike prior studies that used a heating tendency and no microphysics (Markowski and Richardson 2014; Fischer and Dahl 2020), the heating tendency here is added to any condensational/freezing effects from the microphysics scheme. This is not ideal, but based on the ensuing analysis, this combination of effects yields the desired gradual updraft evolution while limiting thermodynamic perturbations outside the developing storm. Cross sections during the tendency nudging phases of the weakest- and strongest-initiated storms are available in the online supplemental material.[1] Across the range of S_0, the result is a variety of subsequent storm morphologies in the same background environment.[2] These evolutionary differences are the focus of the rest of the paper.

c. *Automated storm tracking and motion*

We used an automated technique to track the location of the right-moving supercell in each simulation. A primary midlevel updraft formed by around t = 75 min in each simulation (Fig. 3), which was subsequently tracked from t = 75–240 min. At each 5-min output interval, we found the horizontal area bounded by a contour equal to the 99.98th percentile of the 6-km AGL vertical velocity distribution; over the course of all simulations, this threshold ranged from around 15 m s^{-1} at earlier times to 48 m s^{-1} once the updrafts matured. The updraft center was defined as (x_m, y_m), where each coordinate represents the median in its respective direction. Storm motions were calculated using four-point moving weighted averages of these updraft-center locations. Motions computed from the two closest (in time) updraft locations contributed 40% of the total storm-motion calculation each, and motions computed from the next two closest updraft locations contributed 10% of the total storm calculation each. For example, at t = 100 min, the storm motion in the x direction was computed as

$$c_{x,100} = [0.1(x_{95} - x_{90}) + 0.4(x_{100} - x_{95}) + 0.4(x_{105} - x_{100}) + 0.1(x_{110} - x_{105})] \times \frac{dx}{dt},$$

where $c_{x,100}$ (m s^{-1}) is the u component of storm motion at t = 100 min, x_t is the gridpoint location of the updraft in the x direction at time t (min), dx is the horizontal grid spacing (250 m), and dt is the time interval between model output (300 s). Storm motion was set to 0 m s^{-1} at all times prior to t = 75 min, and the "updraft location" was set to the automated location at t = 75 min, which is consistent with the presence of essentially stationary developing updrafts during this period. Slight variations in the automated updraft location and storm-motion algorithms, including subjective tracking by the first author, yielded negligible variations in the subsequent analysis.

3. Results

a. *General differences in storm-scale characteristics and evolution*

The techniques described above yielded six different supercells evolving in the same background environment. Time series of some selected storm attributes, including minimum

[1] These figures are plotted similarly to the vertical cross sections shown later, but the velocity vectors are plotted less frequently and density potential temperature perturbation contours begin at 0.5 K.

[2] The lower bound of this range (0.016 K s^{-1}) is the minimum heating tendency that produces a supercell in this environment. Beyond the upper bound (0.021 K s^{-1}), we hypothesize that developing supercell updrafts will rapidly foster the (mostly unrealistic) development of barotropic surface vortices around t = 75–90 min (e.g., Fig. 3) prior to cold pool development.

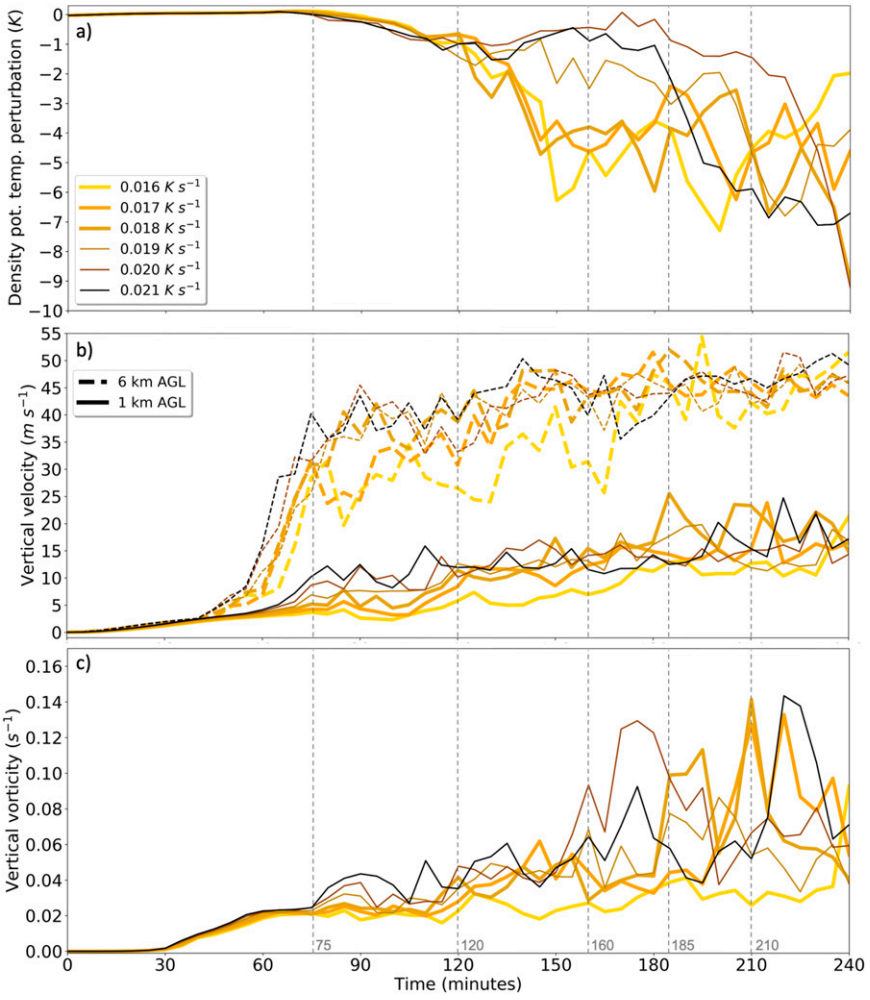

FIG. 3. Time series of (a) minimum density potential temperature perturbation, (b) maximum vertical velocity, and (c) maximum vertical vorticity for each simulation. The maxima and minima are calculated every 5 min in a moving 25 km × 25 km box centered on the midlevel updraft. Potential temperature and vertical vorticity time series are calculated at the lowest model level, and vertical velocity time series are calculated at 1 and 6 km AGL (solid and dashed lines, respectively). Vertical dashed lines, labeled in (c), represent the times at which selected storm attributes are plotted in Figs. 5–8, below. The thicker lines indicate the S_0 = 0.016–0.018 K s^{-1} simulations, and the thinner lines indicate the S_0 = 0.019–0.021 K s^{-1} simulations.

surface[3] potential temperature, maximum surface vertical vorticity, and maximum 1- and 6-km vertical velocity, are shown in Fig. 3. The extremes are calculated in a moving 25 km × 25 km box centered on the 6-km updraft of the right-moving supercell (i.e., the same spatial area plotted in Fig. 4). During the first hour, vertical velocity and surface vertical vorticity slowly increase in response to the tendency nudging in each simulation. They increase slightly faster with larger S_0, but these differences are very small during this time. The positive 10-m AGL vertical vorticity tendency is likely due to the weak tilting of environmental and frictional horizontal vorticities. The formation of quasi-discrete initiation attempts ultimately merging into a more cohesive updraft was relatively common (e.g., Lasher-Trapp et al. 2021). More rapid updraft strengthening occurred in all simulations between t = 60 and 75 min and yielded a persistent midlevel updraft for the remainder of each simulation (Fig. 3b). Simulations with larger S_0 exhibit midlevel updraft strengthening slightly earlier than those with smaller S_0, and they reach slightly larger vertical velocities (e.g., 35–40 m s^{-1}) for the first 2 h of the simulations than those with smaller S_0 (e.g., 30–35 m s^{-1}).

By t = 75–135 min, mid- and low-level updrafts continue to gradually strengthen as the storms develop. At the end of this time period (t = 130–150 min), surface cold pools develop in

[3] Herein, when referring to model output, "surface" refers to the lowest model level (10 m AGL).

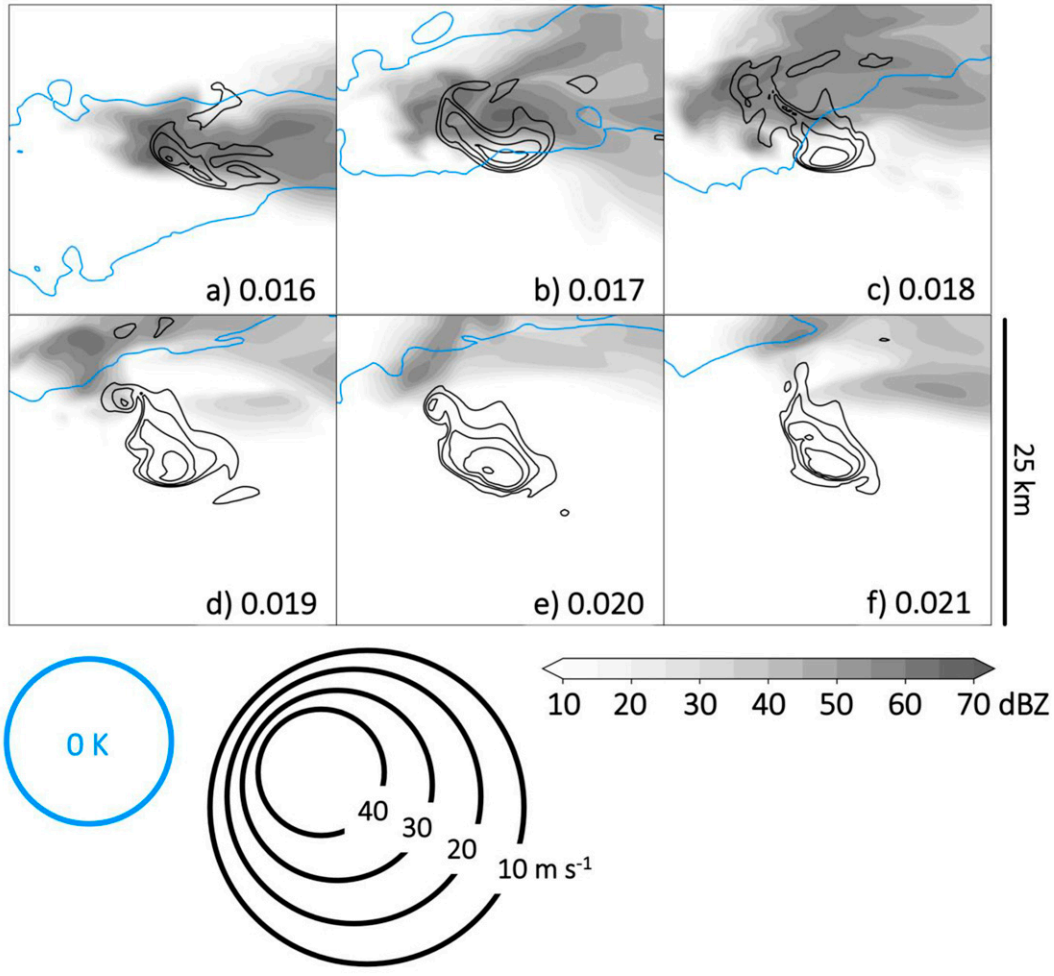

FIG. 4. Surface reflectivity (shaded), 0-K density potential temperature perturbation (blue contour), and 6-km AGL vertical velocities (black contours) at $t = 150$ min for the six simulations.

the weaker-S_0 simulations (herein referring to the simulations with $S_0 = 0.016$–0.018 K s^{-1}). This is an important evolutionary characteristic that seems to discriminate the weaker-S_0 simulations from the larger-S_0 simulations (herein referring to the simulations with $S_0 = 0.019$–0.021 K s^{-1}). As shown in Figs. 4a–c, all of the weaker-S_0 simulations contain a surface cold pool at least partially spreading beneath the midlevel updraft by $t = 150$ min. Conversely, at this time, the larger-S_0 simulations feature a cold pool that is well removed from the midlevel updraft (Figs. 4d–f). This difference is associated with the weaker-S_0 simulations containing strong near-surface downdrafts and the associated divergence and colder air (circled in Figs. 5a–c), whereas the larger-S_0 simulations do not (Figs. 5d–f). Different simulated storm motions and the subsequently different storm-relative wind profiles likely influence these characteristics via differential hydrometeor advection.

Some key differences between the simulations with weakest ($S_0 = 0.016$ K s^{-1}) and strongest ($S_0 = 0.021$ K s^{-1}) thermal forcing are evident in vertical cross sections through the developing storms (Fig. 6). In particular, at $t = 75$ min (the beginning of automated storm tracking in all cases and at the very end of the tendency nudging period), the 0.016 K s^{-1} storm features a relatively narrow tilted 3–9-km (i.e., "midlevel") updraft characterized by peak vertical velocities around 30 m s^{-1} and 3-km vertical velocities around 2 m s^{-1} (Fig. 6a). Meanwhile, the 0.021 K s^{-1} updraft is more vertically oriented and contains peak vertical velocities in excess of 40 m s^{-1} (Fig. 6b). These are driven by differences in the prescribed S_0, yielding maximum density potential temperature perturbations θ'_ρ around 4–6 K in the 0.016 K s^{1} simulation and around 10 K in the 0.021 K s^{-1} simulation. At this time, all precipitation created by the updraft in the x–z cross section remains lofted above 1–2 km AGL and even slightly higher in the 0.016 K s^{-1} run.

Updraft evolution and precipitation fallout—relative to the primary updraft—become critical differences in storm-scale evolution after this point (Fig. 7). By $t = 120$ min, the midlevel updraft in the 0.016 K s^{-1} run has widened slightly and deepened both aloft (extending to around 12 km AGL) and at low levels (Fig. 7a; 2 m s^{-1} vertical velocity extending to

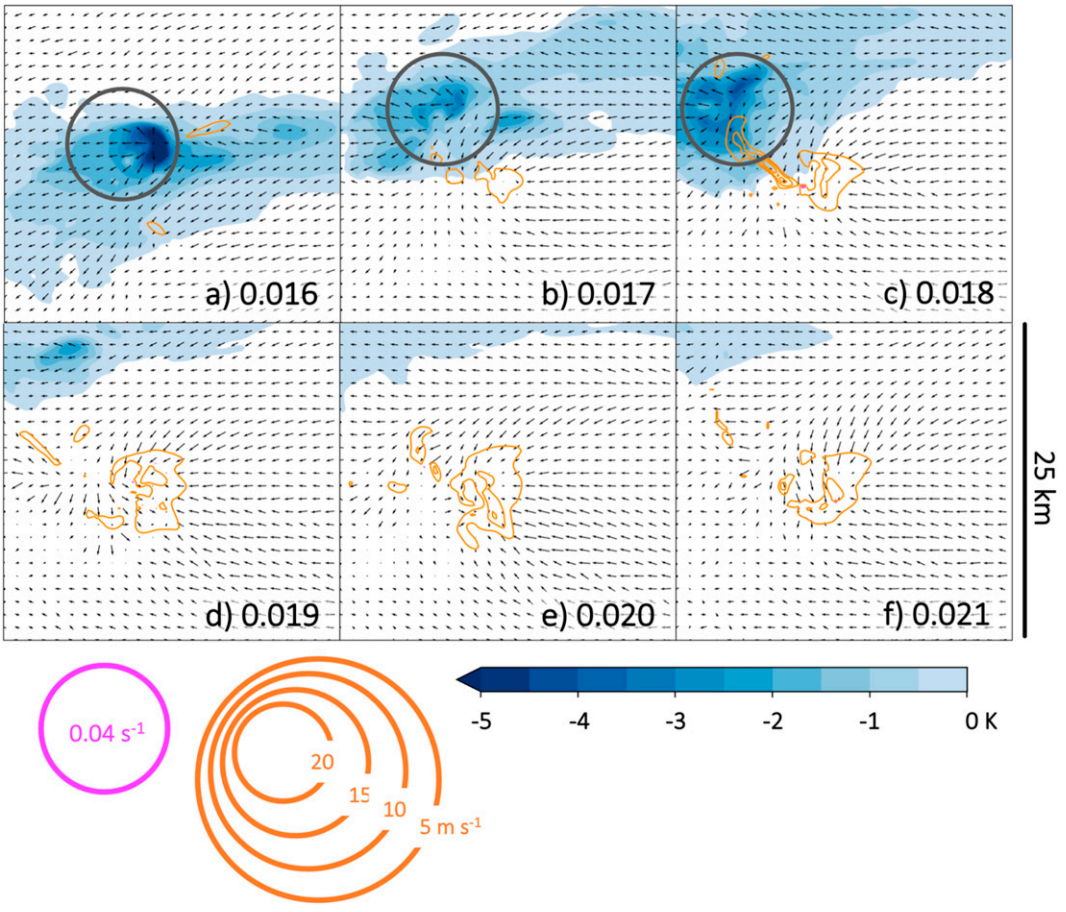

FIG. 5. As in Fig. 4, but with surface density potential temperature perturbation (blue shading), surface vertical vorticity exceeding 0.04 $s,^{1}$ [pink shading in (c)], 1-km AGL vertical velocity (orange contours), and surface storm-relative winds (vectors). Regions containing the coldest surface air and strong divergence are circled in (a)–(c).

around 1.5–2 km AGL). It is also more erect and, consistent with Fig. 3b, has not strengthened much during the time period (with peak velocities maintained around 30 m s^{-1}). In the 0.021 K s^{-1} run, the core of the midlevel updraft (i.e., >20 m s^{-1} vertical velocity) is much wider and extends much closer to the surface, with 10 m s^{-1} updrafts present at 1 km AGL (Figs. 3b and 7b). The different updraft characteristics are associated with different precipitation patterns. This is mostly evident in the vertical cross sections in Fig. 7. While both storms contain similar peak reflectivity values at the surface (horizontal cross sections in Fig. 7), precipitation fallout in the 0.021 K s^{-1} simulation is oriented more downshear from the midlevel updraft (i.e., not as visible in the x/z cross section) than in the 0.016 K s^{-1} simulation. These variations are likely driven by differential hydrometeor advection from stronger updraft-relative flow in the 0.021 K s^{-1} simulation, and vice versa in the 0.016 K s^{-1} simulation. The differences in updraft-relative flow are not associated with different ground-relative wind profiles but rather different storm motions that are already evident based on the grid-relative locations of the updrafts in Fig. 7 (this will be discussed in more detail later). While we do not show cross sections from the 0.018 and 0.019 K s^{-1} runs (for brevity), they generally align with the updraft and reflectivity trends evident in the 0.016 and 0.021 K s^{-1} runs; as such, we believe that the somewhat stark differences between the 0.018 and 0.019 K s^{-1} runs—in terms of near-surface downdraft and cold pool production (Figs. 4 and 5)—represent less of a "step function" and more of an "inflection point" in the parameter space where CI-influenced differences in storm motion quickly become more important for supercell evolution.

Over the next 30–40 min, the presence of precipitation and associated cooling processes closer to the primary updraft (Fig. 7) yields the more established low-level downdrafts and surface cold pools spreading beneath low-level updrafts (Fig. 5) earlier in the more weakly forced simulations in comparison with the more strongly forced simulations (Fig. 3). The strong near-surface downdrafts foster vertical alignment between the cold pool edge, low-level updraft (Figs. 5a–c), and midlevel updraft (Figs. 4a–c) in the weaker-S_0 simulations. Near-surface downdrafts and colder air eventually spread beneath the midlevel updrafts in the larger-S_0 simulations around t = 180–210 min, but some surface vorticity intensification occurs before then (e.g., Fig. 3c at t = 170–175 min for the 0.020 and 0.021 K s^{-1} simulations). The development of this vortex is discussed in more detail in section 3c.

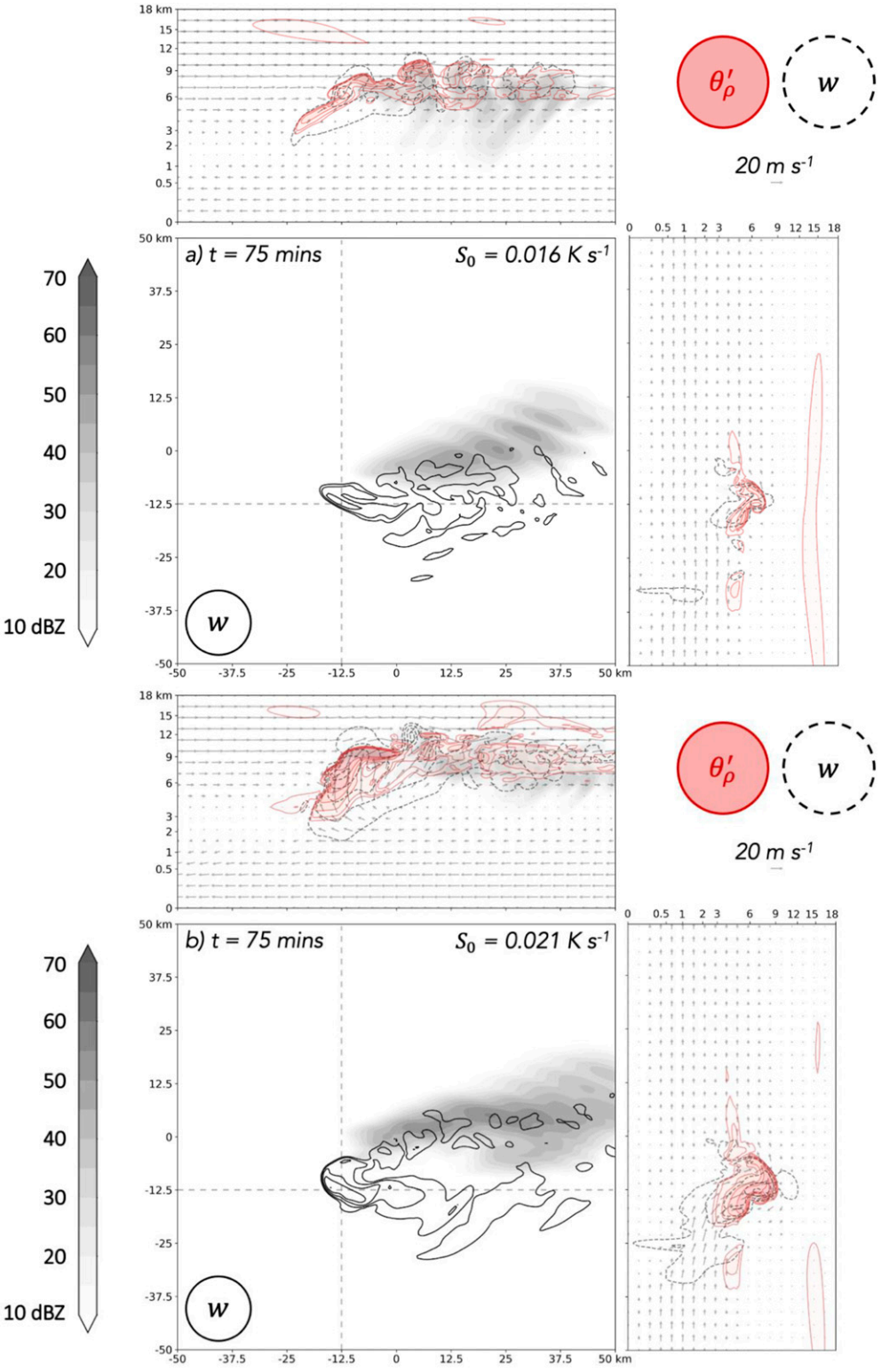

FIG. 6. Storm-scale horizontal and vertical cross sections at t = 75 min (the beginning of storm tracking) for the (a) 0.016 K s^{-1} simulation and (b) 0.021 K s^{-1} simulation. The horizontal cross sections show surface reflectivity (shaded) and 6-km vertical velocity (solid contours every 10 m s^{-1} from 10 to –40 m s^{-1}). A storm-following domain (50 km × 50 km) is shown. The dashed lines indicate the location of the vertical cross

For the remainder of the simulations (i.e., t = 150–240 min), mid- and low-level vertical velocities continue to slowly increase (Fig. 3b). This is especially true for the simulations with weaker S_0, such that by the t = 3–4-h period, maximum vertical velocities are relatively consistent across all ensemble members. Surface cold pool boundaries are in vertical alignment with the midlevel updraft by the end of this time period in all members, and most members exhibit a peak in surface vertical vorticity magnitude (similar to a TLV in prior studies with slightly smaller horizontal grid spacing). Across the simulations, the time of initial surface vortex development appears to be slightly related to S_0, with larger values of S_0 yielding large surface vertical vorticity more rapidly. The absence of a surface cold pool in the vicinity of some of the larger-S_0 vortices (e.g., Figs. 3a,c at t = 175 min for the 0.020 and 0.021 K s^{-1} simulations) calls into question the physical relatability of this relationship; however, this relationship also appears to hold across the three weaker-S_0 simulations (Fig. 3c). Such a relationship is consistent with more rapid low-level updraft development and larger low-level vertical velocities as S_0 increases across the three weaker-S_0 simulations (Fig. 3b). The next subsection describes storm-scale characteristics of the weaker-S_0 simulations in greater detail at key moments in their lifetimes.

b. *Storm-scale characteristics and evolution in the weaker-S_0 simulations*

Figures 8 and 9 reveal storm-scale characteristics of the weaker-S_0 simulations at the times noted in Fig. 3. In general, these times represent the intensification of the midlevel updraft (t = 75 min), the state of storm-scale features prior to the strongest surface cold pool development (e.g., Fig. 3 at t = 120 min), the same features after the arrival of the cold pool beneath the low- and midlevel updrafts (t = 160 min), the first time of large surface vertical vorticity development in any weak-S_0 member (t = 185 min in the 0.018 K s^{-1} run), and the next time of large surface vertical vorticity development (t = 210 min in the 0.017 and 0.018 K s^{-1} runs). At t = 75 min, each member contains an elongated midlevel updraft and downshear precipitation (Figs. 8a–c). By t = 120 min, the midlevel updrafts have expanded in size (particularly in the 0.017 and 0.018 K s^{-1} runs) and surface cold pools have formed in response to evaporative cooling (Figs. 8d–f). The distance between the midlevel updraft and surface cold pool edge is greater with larger S_0. A slightly stronger and wider low-level updraft is also evident in simulations with larger S_0 (Figs. 9a–c). By t = 160 min—after the arrival of the downdraft (e.g., Figs. 5a–c)—larger differences are evident between each simulation. In the 0.016 K s^{-1} run, the surface cold pool has spread beneath the entire midlevel (Fig. 8g) and low-level (Fig. 9d) updrafts. Conversely, in the 0.018 K s^{-1} run, the surface cold pool bounds the bulk of the mid- (Fig. 8i) and low-level (Fig. 9f) updrafts on the upshear side. We reiterate that this difference is not due to variations in the low-level environmental ground-relative wind profile but rather to differences in storm-scale evolution influenced by the strength of thermal forcing for CI (and thus the storm-relative wind profile and, perhaps, differences in precipitation distribution). The influence of the different storm-relative wind profiles from varying storm motions is discussed in section 3d.

By the time of initial surface vortex development (t = 185 min), the 0.018 K s^{-1} simulation features a well-developed cold pool, arcing low-level updraft (Fig. 9i), and vertically aligned updraft structure (Figs. 8l and 9i). Despite their more negatively buoyant cold pools at t = 160 min, the cold pools in the 0.016 and 0.017 K s^{-1} runs are much less negatively buoyant (i.e., perturbations closer to 0 K or positive; Figs. 9g,h) by t = 185 min. At the time of initial vortex formation in the 0.017 K s^{-1} run (t = 210 min), the 0.017 K s^{-1} run features colder outflow in the vicinity of the low-level updraft than the other two members (Figs. 9j–l). By this point, midlevel updraft vertical velocities are similar (Fig. 3b), but the 0.017 K s^{-1} run features a slightly more symmetrical updraft than the other two members (Figs. 8m–o). Last, surface vertical vorticity increases at the very end of the simulation period (i.e., t = 240 min) in the 0.016 K s^{-1} run, at which point it contains storm-scale features like the other two members at their respective times of initial vortex genesis (not shown).

Thus, in these simulations, the developmental time scales of some storm-scale characteristics supporting surface vortex formation (e.g., low-level updraft development, low-/midlevel updraft alignment) are related to the strength of thermal forcing for CI. We are intrigued that in identical background environments, stronger or weaker convection initiation may "push" the storm toward faster (but not necessarily more intense) vertical vorticity development or vice versa. Still, the timing and intensity of surface vortices are likely influenced to some degree by storm-scale stochasticity (or, in other words, highly nonlinear internal processes influencing tornado production that are at best tenuously related to the background environment and therefore practically—if not intrinsically—unpredictable).

c. *Storm-scale characteristics and evolution in the larger-S_0 simulations*

We next perform the same analysis for the larger-S_0 simulations, which featured a different cold pool evolution during the developmental stages of the supercells than the smaller-S_0 simulations (as summarized in Fig. 4). At t = 75 min, midlevel updrafts and precipitation patterns are similar to those in the smaller-S_0 runs (Figs. 8a–c; cf. Figs. 10a–c). Evaporative cooling at the surface from forward-flank precipitation is just

←
sections through the storm location derived from the 6-km updraft. The x–z cross section is shown above each horizontal cross section, and the y–z cross section is shown to the right. In these vertical cross sections, reflectivity is shaded, vertical velocity is contoured (dashed black lines contoured at 2, 10, 20, 30, and 40 m s^{-1}), and density potential temperature perturbations θ'_ρ are contoured and shaded (red solid lines and fill every 2 K, from 2 to –10 K as well as 1 K). Storm-relative velocities in each plane are also shown.

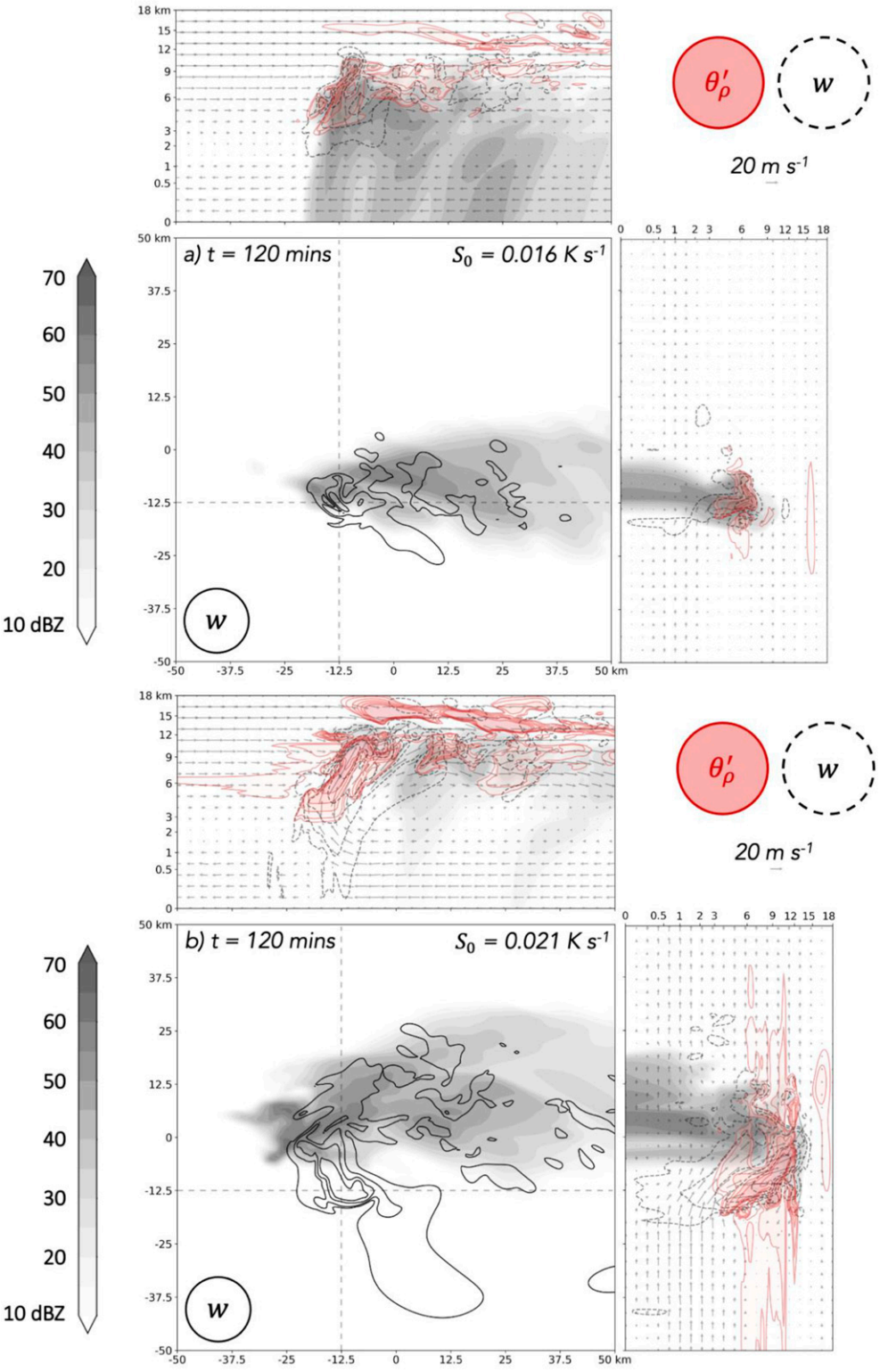

FIG. 7. As in Fig. 6, but at t = 120 min.

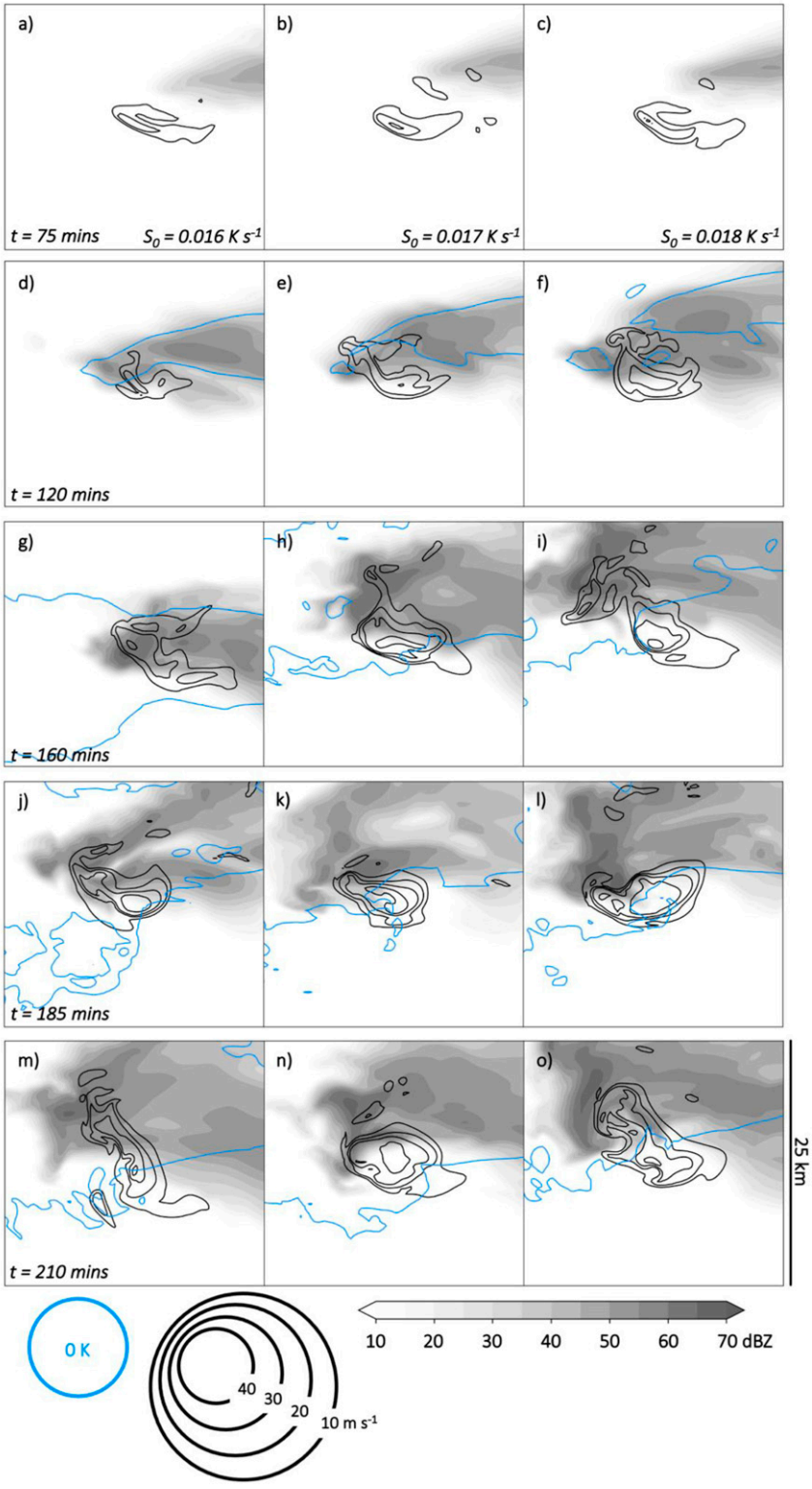

FIG. 8. Surface reflectivity (shaded), 0-K density potential temperature perturbation (blue contour), and 6-km AGL vertical velocities (black contours) at select times for the S_0 = 0.016–0.018 K s.^{1} simulations. The panels are organized by time (rows) and simulation (columns).

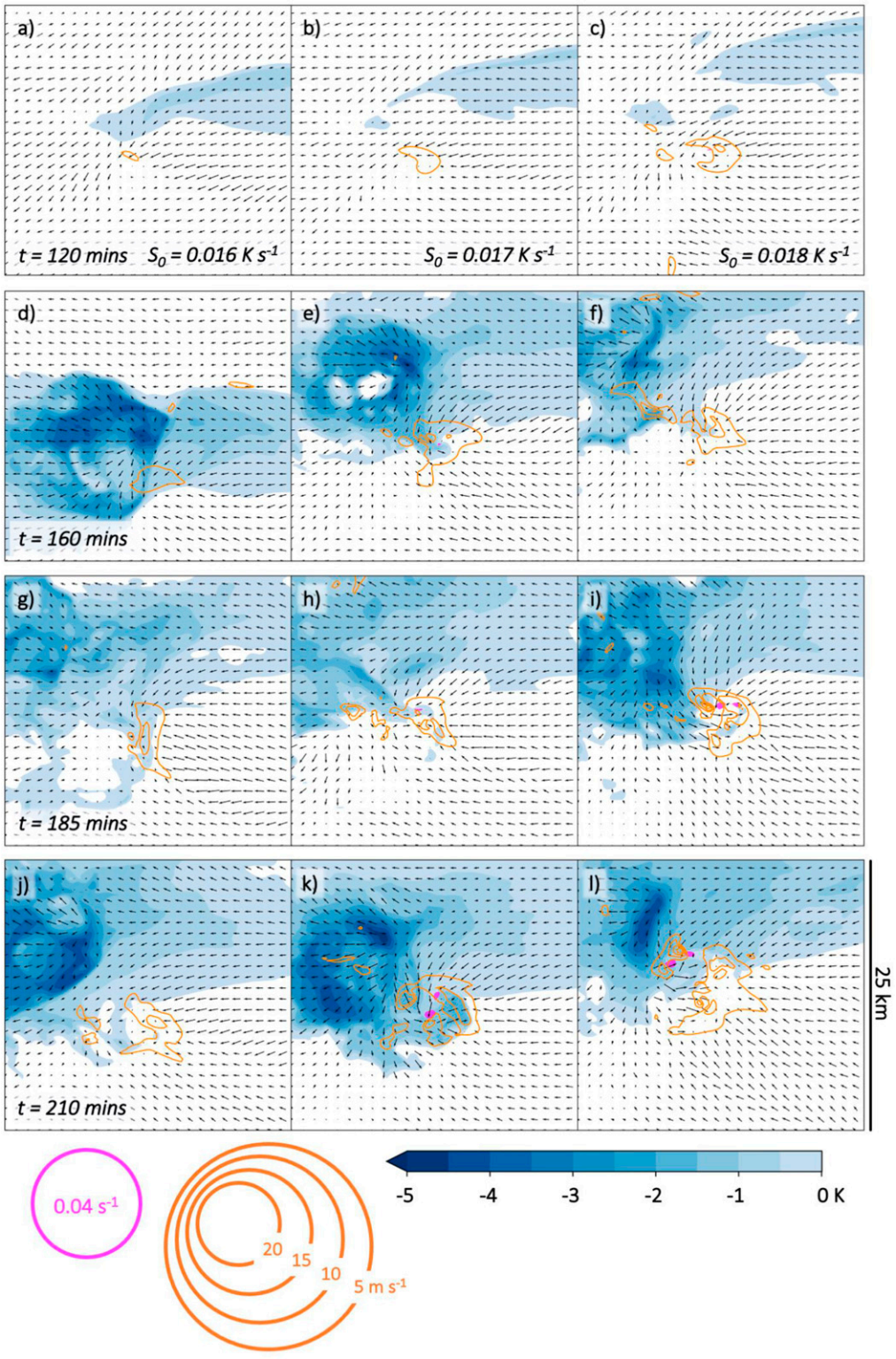

FIG. 9. As in Fig. 8, but with surface density potential temperature perturbation (blue shading), surface vertical vorticity exceeding 0.04 s^{-1} (pink shading), 1-km AGL vertical velocity (orange contours), and surface storm-relative winds (vectors); t = 75 min is omitted from this figure because no potential temperature perturbations or strong 1-km AGL vertical velocities are present at that time.

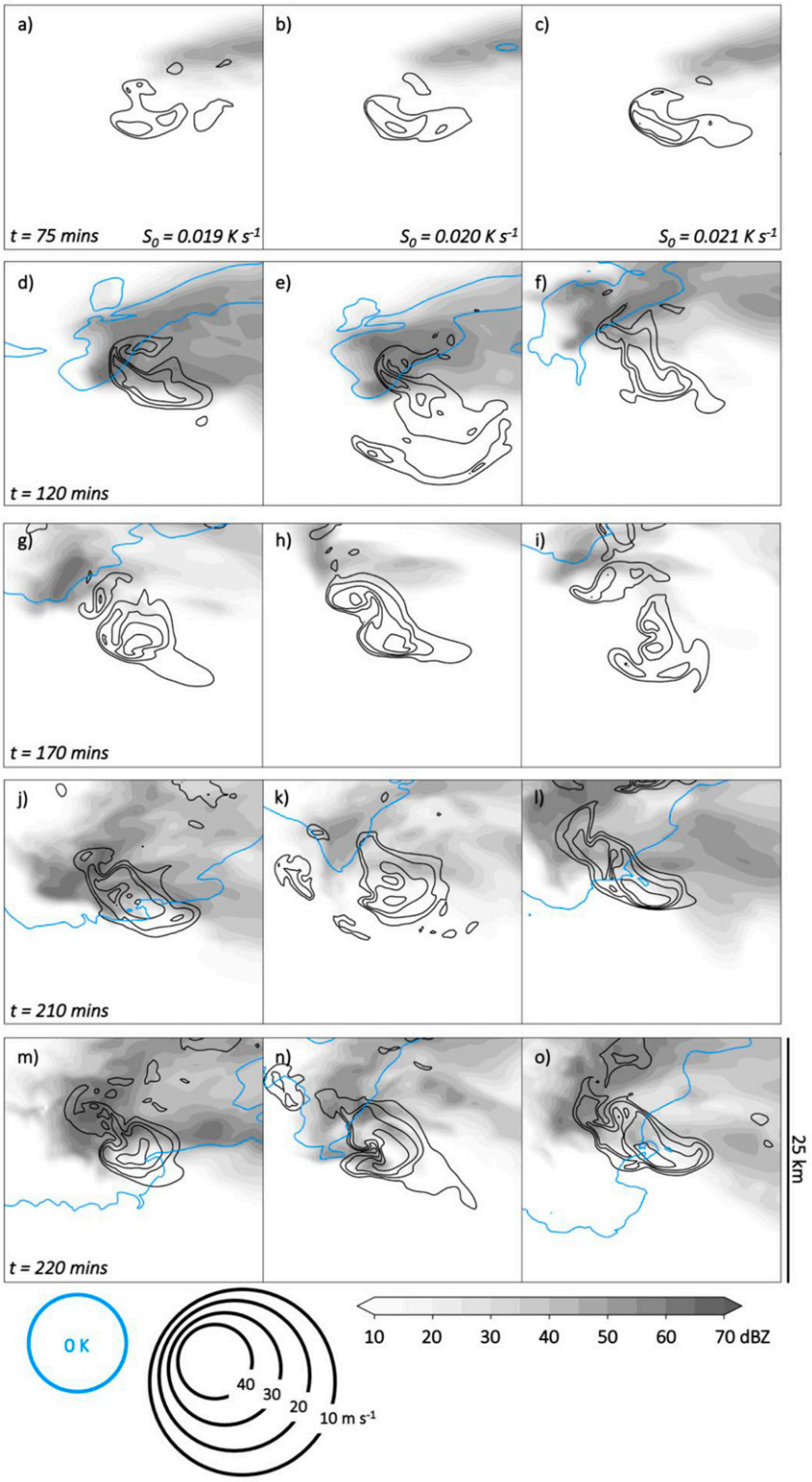

FIG. 10. As in Fig. 8, but for the S_0 = 0.019–0.021 K s^{-1} simulations at t = 75, 120, 170, 210, and 220 min.

beginning in the larger-S_0 simulations by this time (Figs. 10a–c). By $t = 120$ min, precipitation and surface cold pools are generally more widespread in the larger-S_0 simulations than in the smaller-S_0 simulations (Figs. 6–11). The largest differences are evident at $t = 160$–170 min, as the midlevel updrafts in the larger-S_0 simulations become well separated from the main precipitation region. This is due to the delayed arrival of the primary downdraft, as discussed above (Figs. 5–7), and increasingly rightward updraft motion and propagation at least partially associated with updraft cycling (discussed more later). After colder air reaches the ground in the vicinity of the mid- and low-level updrafts (at least in the 0.019 and 0.021 K s^{-1} simulations; Figs. 10j–l and 11g–i), storm structures more closely resemble "classic" supercells for the remainder of the simulations.

A strong vortex forms in the 0.020 K s^{-1} simulation around $t = 170$ min in the absence of local storm-cooled outflow (Fig. 11e). Although identifying vortex-scale processes instigating vortex genesis is beyond the scope (and resolution) of this study, we assessed storm-scale characteristics in the time period leading up to the formation of this vortex and the degree to which they may resemble the nonbaroclinic processes noted in section 1 (in which vortex formation occurs before the formation of storm outflow and gust fronts). Based on our analysis (Fig. 12), we believe that the evolution depicted here is more "realistic" (i.e., including nonbarotropic influences); there is storm outflow in the vicinity of the vortex, but it is warm relative to the background environment (e.g., Fig. 3a). At $t = 150$ min (20 min prior to vortex genesis at $t = 170$ min), chaotic surface flow is present beneath the low-level updraft and is characterized by relatively weak storm-relative flow and sometimes large horizontal vorticity at 110 m AGL (Fig. 12a). A storm-scale downdraft is generally present at 1 km AGL to the northwest of the developing vortex throughout the 20-min time period. Meanwhile, environmental inflow is relatively laminar and, especially within the forward-flank region, is mostly streamwise at 110 m AGL.[4] During the next 10 min, an east–west band of larger surface vertical vorticity develops in the forward flank and is bounded to the north by large streamwise horizontal vorticity aloft. From $t = 155$–165 min, this feature elongates along the storm-relative flow and is connected to the developing vortex (at least with respect to the surface vertical vorticity field; Figs. 12b–d). Within this flow, horizontal vorticity at 110 m AGL is roughly one order of magnitude larger than the surface vertical vorticity. These kinematic characteristics aloft are reminiscent of the streamwise vorticity current noted in past numerical simulations (e.g., Orf et al. 2017) and in some observations (e.g., Schueth et al. 2021) of mature supercells. Furthermore, the turbulent motions present within storm outflow here (e.g., Fig. 12e) differ from the laminar kinematic fields present during premature vortex genesis in recent higher-resolution simulations in the absence of storm outflow (see Fig. 4a in Markowski 2016), and the slightly warm temperatures (~1-K density potential temperature perturbation) near the vortex resemble some field observations in the vicinity of tornadoes (e.g., Markowski et al. 2002; Grzych et al. 2007). While we do not assess the relevant processes in this simulation, the warmer outflow could be driven by forced descent (e.g., Grzych et al. 2007), perhaps due to small-scale pressure gradients associated with internal surges or the deepening surface vortex (e.g., Skinner et al. 2015), or could be reminiscent of a turbulent wake like that discussed in Riganti and Houston (2017). For these reasons, we believe this simulation depicts vortex-genesis processes that are more representative of observed supercells—perhaps cycling or low-precipitation supercells based on the presentation in Fig. 10h—as opposed to those associated with premature vortex genesis.

d. *Differences in storm motion and associated environmental parameters*

Although the environments in all simulations were identical, storm motion varied notably based on the strength of thermal forcing for CI. Figure 13 shows how storm motion varied in time for the 0.016, 0.018, and 0.021 K s^{-1} simulations. In an attempt to not clutter the u/v space, we plot storm motions for only these three simulations every 30 min. By the end of the period ($t = 240$ min), each storm exhibits a motion close to (or more deviant than) Bunkers-right storm motion (Bunkers et al. 2000). Differences between the storm motions are much more evident during the earlier phases of their life cycles. At $t = 75$ min, storm motions vary widely between the three storms. In the case of $S_0 = 0.016$ K s^{-1}, initial storm motion is well to the left of Bunkers-right storm motion (as would be expected) and also slightly to the left of and much slower than the two-thirds 0–6-km mean wind estimate of initial cell motion (Flournoy et al. 2021). At 30–60 min after initiation, the storm motion is closer to the initial estimate and then turns to the right, closer to (or past) Bunkers-right storm motion thereafter. In the $S_0 = 0.018$ K s^{-1} simulation, the storm motion during the first 30 min after initiation is generally left and much slower than the initial estimate. It rotates quickly around to motions closer to Bunkers-right storm motion and oscillates around the origin for the remainder of the experiment. Last, the $S_0 = 0.021$ K s^{-1} storm exhibits a storm motion closer to Bunkers-right storm motion immediately upon CI. Furthermore, it maintains a relatively constant storm motion that is near Bunkers-right storm motion for its entire life cycle. These differences may partially explain why Flournoy et al. (2021)—who examined observed characteristics of 220 supercells presumably across a breadth of thermal forcing strengths—failed to find significant relationships between environmental parameters and storm-scale characteristics like the time of the right turn; the variations in the strength of CI forcing could not be quantified in that study.

The positive relationship between initiation strength and immediate rightward deviance is consistent with the theory relating storm propagation to the vertical velocity field. Storm motion is ultimately a combination of 1) advection by the mean wind and 2) upward forcing that is displaced from the current updraft location or propagation (e.g., due to updraft and/or cold

[4] Horizontal vorticity is mostly crosswise everywhere within the 10–100-m AGL layer because of the inclusion of surface friction (not shown) and becomes streamwise more rapidly with height in regions with large streamwise vorticity at 110 m AGL (as shown in Fig. 12).

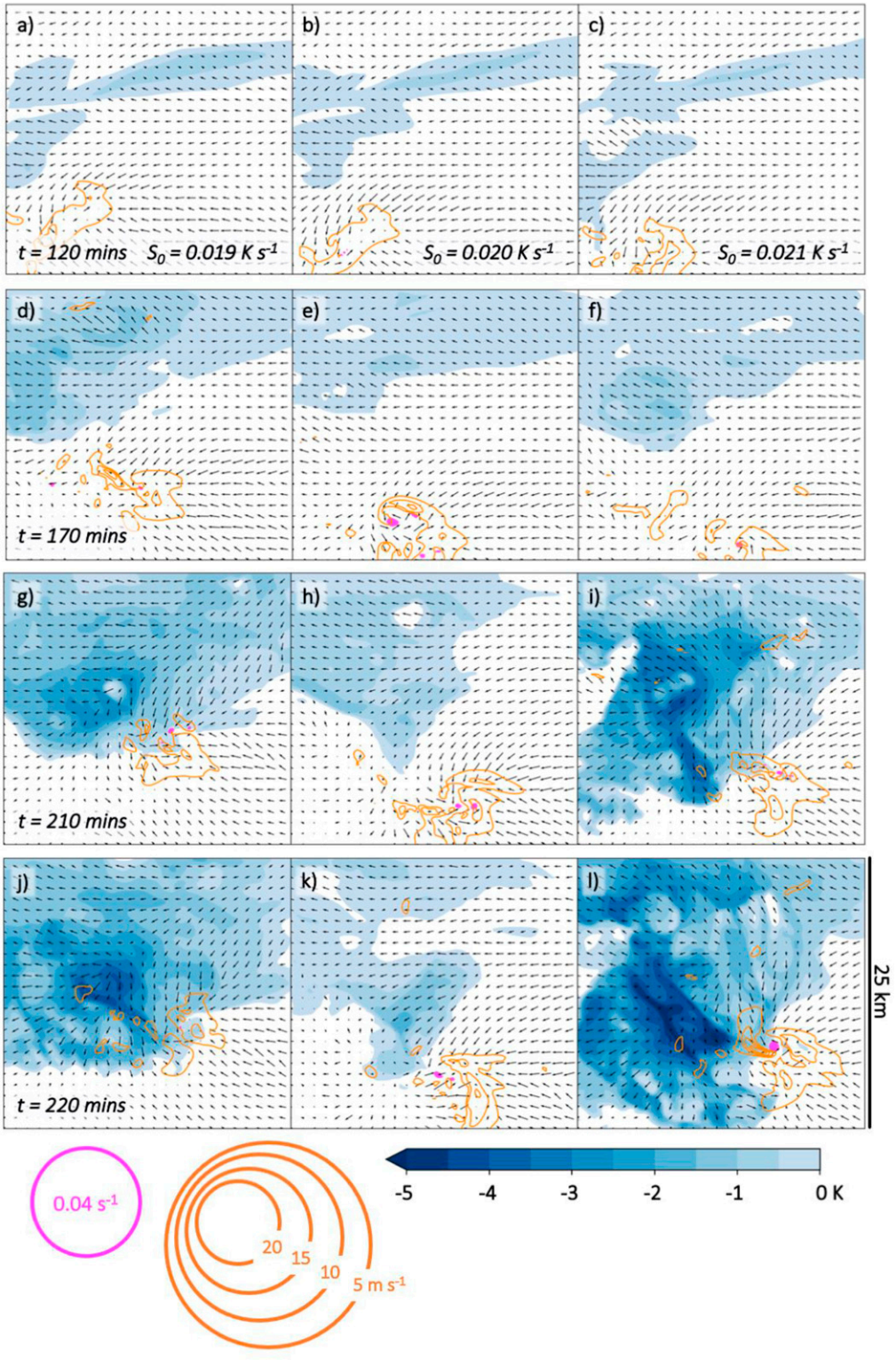

FIG. 11. As in Fig. 9, but for the S_0 = 0.019–0.021 K s^{-1} simulations at t = 120, 170, 210, and 220 min.

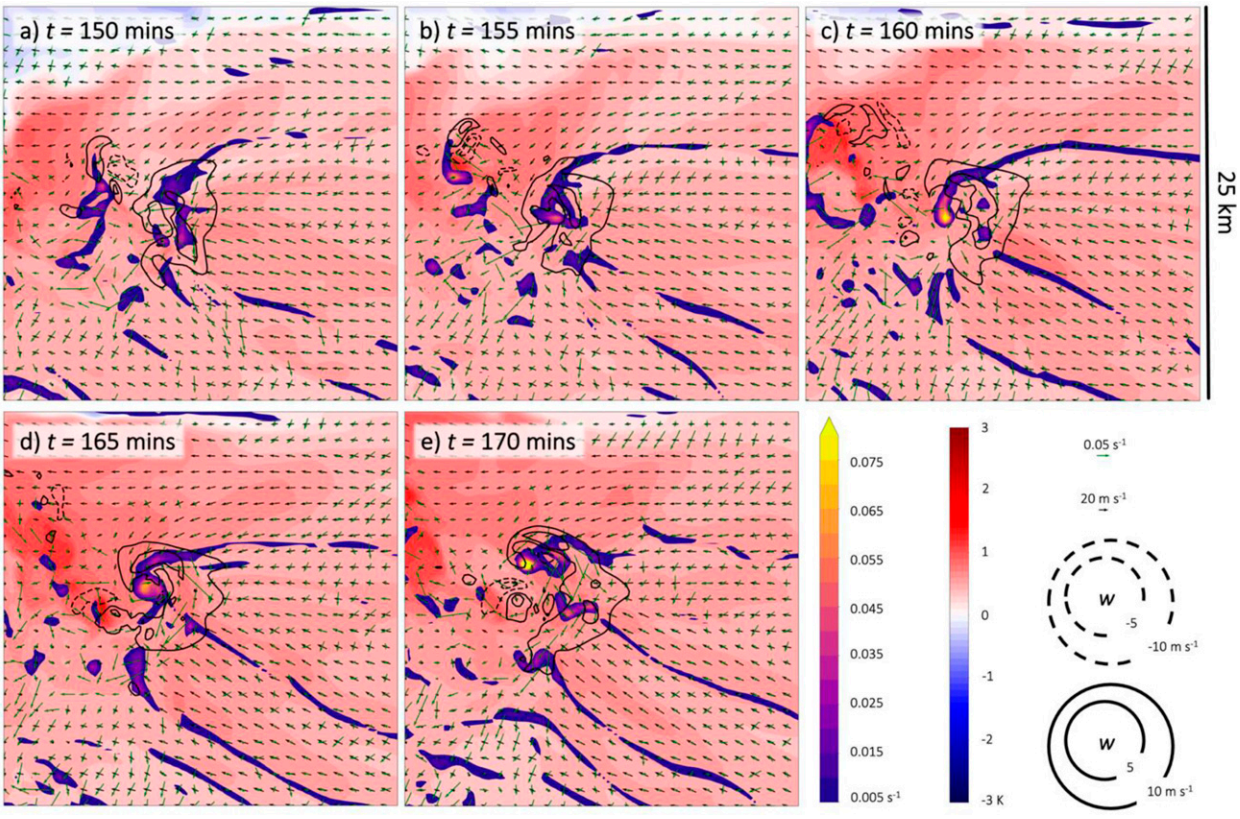

FIG. 12. (a)–(e) Surface density potential temperature perturbation (red/blue fill), surface vertical vorticity (purple/yellow fill), vertical velocity at 1 km AGL (dashed and solid black contours), and storm-relative winds (black vectors) and horizontal vorticity (green vectors) at 110 m AGL for t = 150–170 min for the 0.020 K s^{-1} simulation. All plots are centered on the 6-km AGL vertical velocity maximum.

pool processes). Horizontal updraft propagation contains both along-shear and off-shear components and is driven by the vertical gradients in the pressure perturbation field, expressed below as

$$p' \propto (e'_{ij})^2 - \frac{1}{2}|\omega'|^2 + 2\left(\frac{\partial w'}{\partial x}\frac{\partial \overline{u}}{\partial z} + \frac{\partial w'}{\partial y}\frac{\partial \overline{v}}{\partial z}\right) - \frac{\partial B}{\partial z}. \quad (1)$$

In Eq. (1) (Markowski and Richardson 2010), B is the buoyancy, $\overline{u}$ and $\overline{v}$ are the horizontal base-state wind components, w' is the vertical velocity ($\overline{w} = 0$), ω' is the perturbation vorticity, and e'_{ij} is the rate-of-strain tensor for the perturbation winds. Equation (1) is only valid in the case of a horizontally homogeneous environmental wind profile. The first two terms on the rhs of Eq. (1) represent nonlinear pressure perturbation forcing terms (p'_{NL}), the third term represents the linear pressure perturbation forcing term (p'_L), and the fourth represents the influence of the buoyancy profile. In this framework (e.g., Rotunno and Klemp 1982, 1985; Weisman and Klemp 1984), larger w' implies larger horizontal gradients of w', ultimately yielding larger magnitudes of p', larger vertical gradients of p' on the updraft flanks, and faster storm propagation. In an environment characterized by a straight shear profile, the linear contribution to propagation is directed parallel to the shear vector. In an environment with a veering shear profile like this one, the linear contribution to propagation also contains a component perpendicular and to the right of the shear vector. Furthermore, w' indirectly influences storm propagation by reorienting crosswise barotropic vorticity, leading to vortices associated with p'_{NL}. As the updraft matures, crosswise barotropic vorticity is tilted upward to create a dipole of oppositely signed vorticity maxima aloft along the flanks of the updraft to the left and right of the shear vector; by Eq. (1), both of these vorticity maxima are associated with negative p' and subsequently induce positive vertical velocity tendencies beneath them (Rotunno and Klemp 1985). This yields a rightward-propagating cyclonic storm motion to the right of the shear vector (Rotunno and Klemp 1982). Stronger w' will directly influence additional storm-scale processes that ultimately beget a stronger and/or more deviant updraft, including 1) increased vertical vorticity aloft via stretching, which in turn generates more negative p'_{NL} aloft, greater $\partial p'_{\mathrm{NL}}/\partial z$, and ultimately a stronger updraft, and 2) a greater initial vertical updraft extent, which in this case yields updraft interaction with increasingly westerly shear, thus yielding more rightward storm motion. Last, stronger storm-relative inflow arising from increasingly deviant motion may yield wider updrafts that are less susceptible to the deleterious influences of entrainment and are capable of further strengthening and deviance (e.g., Peters et al. 2019; Coniglio and Parker 2020).

These differences in storm motion determine the storm tracks shown in Fig. 14. The weaker-S_0 storms take more time

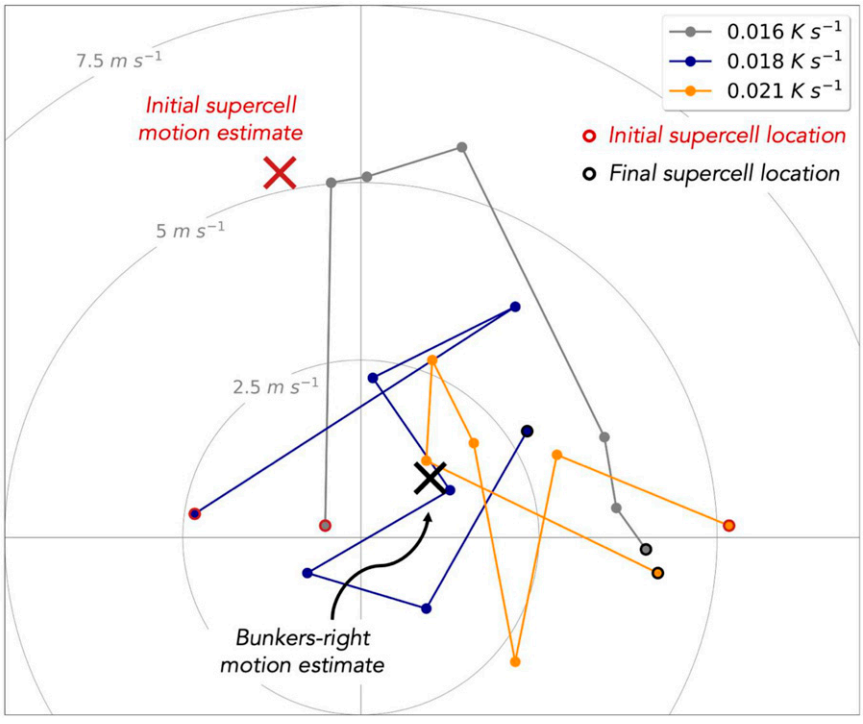

FIG. 13. Time series of storm motions for selected simulations plotted in u–v space. Storm motions are plotted every 30 min beginning at t = 75 min (circles outlined in red) and ending at t = 240 min (circles outlined in black). The two-thirds 0–6-km mean wind estimate of initial cell motion and Bunkers-right storm motion are indicated by the red X and black X, respectively.

to deviate to the right of the shear vector, in this case resulting in faster and more northward storm motions. Conversely, the larger-S_0 storms deviate to the right more quickly, yielding a slower, more consistent storm track generally to the east-northeast. In these experiments, this is due to 1) updrafts strengthening at slightly earlier times in the larger-S_0 runs and 2) the larger-S_0 storms generally achieving greater midlevel vertical velocities around t = 75–120 min. These factors yield greater horizontal gradients in vertical perturbation pressure forcing (Rotunno and Klemp 1982, 1985), contributing to more rapid deviant storm motion in the larger-S_0 storms. Across the range of S_0 examined here (on the weaker side of initiation strengths), this eventually results in differences in storm locations of around 25 km. Such differences could be very important in the presence of environmental inhomogeneities, including mesoscale kinematic and/or thermodynamic gradients (e.g., Markowski et al. 1998; Davenport and Parker 2015; Klees et al. 2016; Gropp and Davenport 2018; Brown et al. 2021), fronts or outflow boundaries (e.g., Magee and Davenport 2020), or cell mergers (Flournoy et al. 2022).

We also observe some unsteadiness in the storm motions (Fig. 13) and subsequent tracks in Fig. 14. There is a slight tendency for weaker-S_0 storms to exhibit more unsteadiness than larger-S_0 storms, which is consistent with the previous discussion regarding smoothed storm motions. Increased smoothing, at some point, would inevitably "wash out" these slight variations in storm motion and track; however, we believe that they may be important indicators of storm evolution on smaller time scales, as has been noted in a recent study of observed supercell motion and tornado production (Coniglio and Parker 2020).

These variations in storm motion directly influence some environmental parameters that are related to storm characteristics, like storm-relative helicity (SRH). Figure 15 shows time series of the range of SRH values in different layers across all six simulations. In these calculations, the environmental shear vector is the same for all simulations, while the storm-relative wind vector and angle between the two changes is in accordance with the time-dependent storm motion. The result is that SRH evolves in time for each storm. Based on Fig. 15, it seems that the range of SRH values in each layer across all simulations remains fairly constant in terms of raw values and spread. The center of the ranges in SRH is close to the SRH value derived from assuming a steady Bunkers-right storm motion (Bunkers et al. 2000). At some times, it appears that the spread in SRH increases with increasing depth (e.g., comparing 0–3-km and 0–0.5-km SRH around t = 130 min). This is due to the large differences in simulated storm motion at that time during the developmental stages of the supercells (see Figs. 13 and 14). Once all of the storms attain a steadier, more deviant storm motion, the spread in 0–3-km SRH decreases (e.g., half an hour later at t = 160 min).

Variations in SRH between different simulations are clearest in Fig. 16; rather than depicting variations in SRH with time as

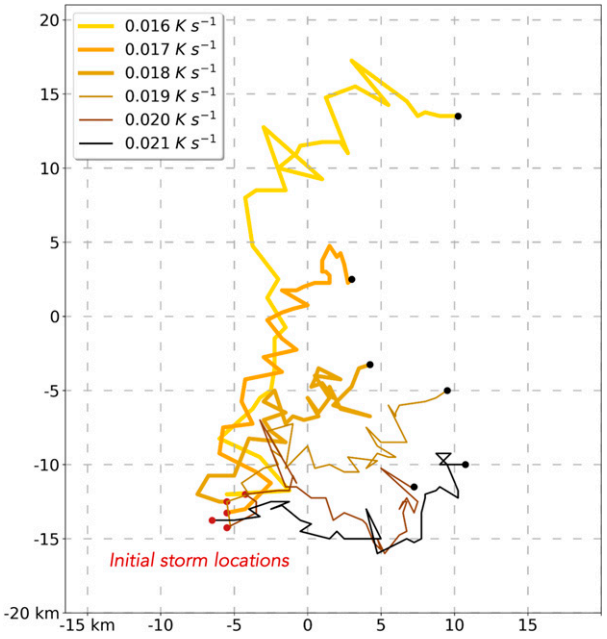

FIG. 14. Storm tracks for each simulation from the onset of an identifiable midlevel updraft (t = 75 min) until the end of the simulation (t = 240 min). The tracks are color coded by simulation. As in Fig. 13, red and black symbols indicate the initial and final locations, respectively, for each storm. The origin of the grid is the center of the domain.

in Fig. 15, Fig. 16 shows the distributions of SRH in different layers in each simulation. Thus, each violin plot incorporates SRH values at all times in the designated layer for the designated simulation. The clearest trend in Fig. 16 is for the medians of each distribution to increase within each layer as S_0 increases. For example, median SRH is larger in all layers in the 0.021 K s^{-1} simulation than in the 0.016 K s^{-1} simulation. This trend is not valid for some pairs of specific simulations (e.g., the 0.017 and 0.018 K s^{-1} runs) but is present when considering the entire S_0 parameter space. Furthermore, some simulations contain greater spreads in SRH than others; for example, the distributions of SRH in all layers in the 0.016 K s^{-1} simulation are greater than any distribution for any other simulation. This is due to the supercell in the 0.016 K s^{-1} simulation exhibiting much larger variance in storm motion during its life cycle than any other storm (e.g., Figs. 13 and 14). Thus, the vertical extent of the violin plots is directly proportional to the time variance in storm motion in each ensemble member. It is smaller for simulations with greater S_0 (e.g., greater than 0.016 K s^{-1}), but it does not appear to steadily diminish as S_0 increases. There is a slight tendency for the intersimulation SRH spread to increase as the depth over which SRH is calculated increases, especially in the first 1–1.5 h after storm tracking begins (in terms of the amount of spread relative to the median values of SRH; consistent with Fig. 15). This suggests that—at least in this background environment—deeper-layer SRH (0–3 km) is slightly more sensitive to increasingly deviant motion than lower-layer SRH (0–500 m); this corroborates the findings of Coniglio and Parker (2020) (their Fig. 11). Finally, Fig. 16 clearly shows that weaker S_0 supported storm motions that generally yielded smaller SRH than that derived from assuming a Bunkers-right storm motion (i.e., the S_0 = 0.016–0.018 K s^{-1} simulations). The opposite is true for larger S_0. This is again directly related to the fact that larger S_0 yielded deviant motions—ultimately more deviant than Bunkers-right storm motion—more rapidly in the storms' life cycles.

4. Discussion

This study provides an additional perspective to some recent work examining the "range of possible outcomes" regarding supercell evolution in a given background environment. Coffer et al. (2017), Flournoy et al. (2020), and Markowski (2020) achieved different storm-scale outcomes by applying very small perturbations to the background wind profile (i.e., within the typical observation error of radiosondes) or the environmental temperature field. Fischer and Dahl (2020) noted small differences in storm-scale characteristics as they varied the maximum heating tendency in their idealized simulations. We believe our

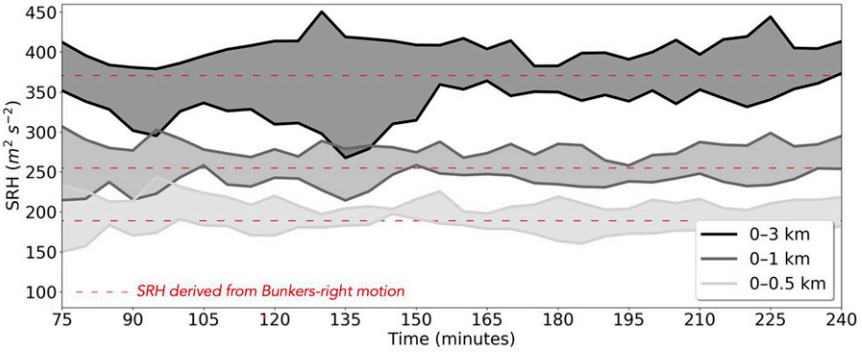

FIG. 15. Time series of the range of 0–0.5- (light gray), 0–1- (gray), and 0–3-km (dark gray) SRH across all six supercells for t = 75–240 min. The environmental shear profile is constant for the SRH calculations such that variations in SRH are solely due to evolving storm motions. The dashed red lines indicate the SRH values for each layer assuming a steady Bunkers-right storm motion (Bunkers et al. 2000).

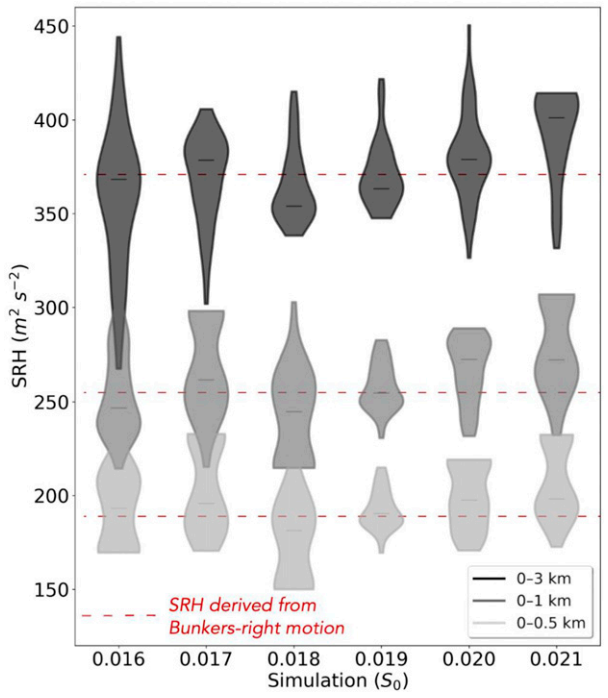

FIG. 16. Violin plots of the distribution of SRH values in the 0–0.5- (light gray), 0–1- (gray), and 0–3-km (dark gray) layers at all time steps for t = 75–240 min in each simulation (marked on the x axis). The median for each distribution is indicated by a horizontal line in the violin. The dashed red lines indicate the SRH values for each layer, assuming a Bunkers-right storm motion (Bunkers et al. 2000).

findings complement these studies [especially Fischer and Dahl (2020)] in showing how altering storm-scale initiation strength, rather than characteristics of the background environment like the wind profile or temperature field, can yield different outcomes and (possibly) extend storm-scale predictive skill on meaningful time scales. As far as we know, this is the first study to focus on differences in storm-scale outcomes, not by randomly altering the background sounding or systematically modifying the background environment, but rather by systematically changing the strength of forcing for CI. We are not sure if one CI method should be preferred over others for exploring this sensitivity of outcomes. Rather, we highlight this novelty as another small step away from rigidly assigning storm-scale outcomes based on an environmental sounding and toward examining the variability of storm-scale evolution in time within a fixed environment.

In terms of the time dependency of storm evolution, it is intriguing that a storm's fate may be strongly influenced by characteristics of its initiation. We found that some observable storm characteristics like initial motion are strongly influenced by the strength of thermal forcing for CI. Furthermore, SRH in the vicinity of the supercells varied greatly based on CI and its subsequent impacts on deviant storm motion. The degree to which these relationships are present in real, more complex supercell initiations (e.g., Ziegler et al. 1997) remains unclear and is worthy of future study. Parcels entering real developing updrafts may reside closer to the surface than those in this study, in which the updraft arose via midlevel heating. We believe that focused investigation of supercell initiation in future field campaigns will help address this topic. If such relationships hold, observing developing convection in supercell environments may yield increased real-time predictive skill hours in the future. We plan to examine whether satellite imagery may be a useful tool for estimating real-time cloud-top vertical motion as a proxy for the strength of forcing for CI. Based on our findings, another useful proxy might be to assess the ensuing storm motion, with storms that initially deviate more to the right being indicative of stronger forcing and being more likely to rapidly mature and produce severe hazards—like tornadoes—more quickly. Hypotheses like these could be tested using the sounding dataset presented in Coniglio and Parker (2020) and others that contain sufficient sounding data to characterize the environment in the vicinity of CI and early supercell evolution. Further, differing motions associated with CI forcing have implications for subsequent storm interactions.

The degree to which the relationships between simulated CI and supercell evolution shown here are represented in the observed atmosphere strongly depends on the realism of our CI technique. The goal of the tendency nudging technique was to portray time scales of observed supercell evolution more realistically (e.g., time from CI to the right turn, surface cold pool production, vortex production). However, the physical ways by which these are manifested in the idealized simulations are probably not as realistic. Real surface-based supercell CI is associated with boundary layer convergence, of which this model contains none. This model also contains artificial heating from the tendency nudging technique as well as heating from parameterized phase changes; while this yields more gradual realistic time scales of supercell evolution, it may not be for the right physical reasons. This naturally poses the question of whether relationships like these, between CI characteristics and subsequent evolution, exist in the real atmosphere.

The large sensitivity of supercell evolution to the strength of thermal forcing for CI also suggests that the manner in which a simulated supercell forms may strongly influence its downstream evolution. Historically, some idealized simulations of supercells (including our own in prior studies) feature very strongly forced CI that yields objectively unrealistic, premature features before evolving toward a more realistic quasi-steady state. We believe that it would be wise for idealized supercell modelers to consider this possibility and incorporate more relaxed CI techniques [like this one or a heat flux method as in Lasher-Trapp et al. (2021)] when possible.

This study focused on supercells forming in an environment very favorable for tornado production. Based on our experiences, other studies, and conversations with colleagues, it is difficult to create a simulated storm in the composite near-field tornadic VORTEX2 profile that does not produce a "tornado" (Coffer and Parker 2017; Coffer et al. 2017; Coffer and Parker 2018; Flournoy et al. 2020). The 0.016 K s^{-1} simulation presented here might be the best example of a

nontornadic storm from this profile so far and suggests there may be other fundamentally important influences on tornado production that are related to a storm's evolutionary path.

As discussed above, the strongest storm in this study featured a relatively constant storm motion during its entire life cycle. To us, it seems that achieving a quasi-steady-state balance between the storm and its local environment might be a ubiquitous characteristic of intense supercells supporting long-lived tornadoes. Based on our findings, achieving such a state more rapidly, at least in volatile environments like this one, appears more likely given stronger forcing for CI.

This study only examines the sensitivity of storm evolution and motion to differences in maximum initiation magnitude. We did not methodically examine other characteristics of initiation, like the vertical location of the maximum tendency nudging, its vertical and horizontal extents, and the time scales associated with its increase and decrease. We leave exploring these sensitivities as well as differences in environmental characteristics for future work.

5. Summary and concluding remarks

Better anticipating storm-scale evolution hours in advance remains an important goal for forecasters and researchers alike. This is especially true for convective events in which the background environment supports both tornadic and nontornadic supercells. How can we better anticipate the evolution of each storm? Are there storm-scale characteristics independent of the background environment that may be useful?

We addressed these questions with respect to CI using six CM1 simulations of supercells evolving in an environment adapted from the composite near-field tornadic VORTEX2 profile. In an effort to capture more gradual updraft development, we used the tendency nudging technique to initiate convection. This method involves adding a positive time-dependent tendency to the potential temperature equation at each time step. Prior studies have used a heating tendency or updraft nudging to achieve initiation, at the expense of "shocking the system"; it seems that these techniques, especially in the presence of a nonfree-slip lower boundary, can quickly yield an intense surface vortex that typically does not occur in real supercells. As we show here, applying a time dependency to the heating tendency helps reduce the initial "shock" and allows for more gradual updraft development in this framework.

Although the background environment in all simulations was identical, the evolutions of the supercells were very different. Mid- and low-level updrafts as well as intense surface vortices developed at different times in each case. Some of the cases featured colder cold pools, stronger low-level updrafts, and more intense surface vortices during the 4-h period than others. This is a testament to the range of storm-scale outcomes that are possible within a given background environment and how they are related to the strength of thermal forcing for CI. This includes storm-scale attributes that were more directly influenced by the systematic changes in CI strength (e.g., low-level updraft strength and the timing of low- and midlevel updraft intensification) and those that were not as directly influenced (e.g., cold pool character and surface vortex production). Our most important findings from these simulations are summarized as follows:

1) Given a homogeneous background environment, the strength of thermal forcing for CI can influence a variety of storm-scale evolutionary paths. In this case, differences in forcing strength yielded different supercell characteristics like storm motion, updraft development, cold pool intensity, and surface vortex production.
2) Stronger thermal forcing is associated with more rapid updraft development. Faster updraft development occurred because larger heating tendencies were intuitively associated with larger vertical velocity tendencies.
3) Stronger thermal forcing may be associated with more rapid surface vertical vorticity development. During the first 2 h, maximum surface vertical vorticity increased faster in simulations with larger S_0. In some cases, this resulted in intense TLV production at earlier times; however, the timing of TLV development was also strongly influenced by other internal (and nonlinear) processes and not solely linked to S_0.
4) Stronger thermal forcing may yield more deviant initial storm motion, more consistent motion throughout the storm's life cycle, and greater SRH earlier in the storm's life cycle. This change in storm motion is likely due to stronger induced vertical velocities influencing the perturbation pressure field and updraft propagation at earlier times. In environments like this one, characterized by vertically veering wind shear that is not perfectly streamwise, both linear and nonlinear pressure perturbations would be expected to contribute to this deviant motion. This can be important in determining storm motion very early in the storm's life cycle, especially with larger forcing for CI.

To our knowledge, this study is the first to show that differences in early evolution can result in widely different subsequent storm evolutionary paths, especially in terms of surface vortex production. Furthermore, we showed how these differences systematically yielded different outcomes—namely, through different CI forcing strengths triggering supercell deviance and updraft development at different times. Numerous questions remain. Using this framework, what is the strongest initiation strength that is feasible while maintaining more realistic early evolution? In this case, how widely do eventual storm locations vary across this range of initiation strengths? Do real supercells exhibit relationships between the strength of forcing for CI and subsequent evolution via the same physical processes? Can observations of storm motion be used in real time to diagnose initiation strength and anticipate subsequent evolution? On the other hand, can observations of initiation help forecasters predict early storm motion and evolution?

These findings expand our knowledge of what processes can result in different storm evolutionary paths within identical environments. This is important for researchers and operational forecasters alike in real-time settings, for example, in trying to anticipate 1) which storms will produce tornadoes

and 2) when each storm will produce tornadoes. In addition to better characterizing the near-storm environment, targeted observation of characteristics of CI may improve forecasts like these. Ultimately, these findings suggest that increased forecast performance up to hours in advance, for example, on the watch-to-warning time scale, can be improved by better understanding CI and its relation to storm development in observed supercell events.

Acknowledgments. We are grateful for George Bryan's continued support of CM1. We thank Mike Coniglio for providing an initial review of the paper, as well as Chris Nowotarski and two other reviewers whose comments greatly improved the paper. We also thank Jimmy Correia, Casey Davenport, Mateusz Taszarek, Luke LeBel, and Greg Blumberg for their insightful comments about previous studies of convection initiation. Funding was provided by the NOAA/Office of Oceanic and Atmospheric Research under NOAA–University of Oklahoma Cooperative Agreements NA16OAR4320115 and NA21OAR4320204, U.S. Department of Commerce. The first author was funded on a postdoctoral fellowship through the Cooperative Institute for Severe and High-Impact Weather Research and Operations. The statements, findings, conclusions, and recommendations are those of the authors and do not necessarily reflect the views of NOAA or the U.S. Department of Commerce.

Data availability statement. CM1 "namelist.input" and "toy.input" files are available online in a GitHub repository ("mdflournoy/tendency-nudging"). Codes used to produce the analyses in this paper are available upon request from the first author.

APPENDIX

Tendency Nudging Convection Initiation Technique

a. Motivation for the tendency nudging technique

Idealized cloud models are a very useful tool for diagnosing relationships between storm-scale characteristics and other aspects of the model, such as the background homogeneous environment, nature of surface friction, and boundary layer characteristics and parameterizations. However, several recent studies of idealized supercells have contained a strong TLV at and near the surface at very early times in the supercells' life cycles prior to the development of any precipitation at the surface or appreciable downdrafts in the storm (Fig. A1). The presence of this TLV is predominantly inconsistent with observations of supercell evolution (Bluestein and Parker 1993; Flournoy et al. 2021). Furthermore, the nonbaroclinic processes by which these TLVs develop (Markowski 2016; Roberts et al. 2016; Roberts and Xue 2017; Davies-Jones 2021) are inconsistent with results from numerical simulations highlighting the importance of baroclinicity in the vorticity budget (e.g., Wicker and Wilhelmson 1995; Dahl et al. 2014; Markowski 2016) and the overwhelming majority of observed supercell tornadoes that are located within storm-cooled outflow (e.g., Markowski et al. 2002; Grzych et al. 2007; Hirth et al. 2008). Some of these TLVs are very strong—at least with respect to subsequent TLV development (e.g., Markowski 2016; Coffer et al. 2017; Flournoy et al. 2020)—while others are weaker (e.g., Fischer and Dahl 2020). Ultimately, it is plausible that this variety of "premature" TLVs may unrealistically impact subsequent supercell simulation.

The glaring question that arises is, if these premature TLVs are not representative of observations, why do they oftentimes develop in idealized supercell simulations? A synthesis of recent simulations focused on surface vertical vorticity development in simulated supercells is presented in Fig. A1. This includes experiments that are known to contain a premature TLV, as well as those in which no premature TLV exists (based on the data presented in each study, e.g., time series of maximum near-surface vertical vorticity), or its presence is unclear based on the data presented in that study. There are no clear relationships between the presence of the premature TLV and certain aspects of each experiment (e.g., grid spacing, initiation scheme, friction), although the sample size is admittedly rather small.

It is possible that premature TLVs are more likely to arise in simulations with excessive near-surface vertical wind shear generated by "invented forces" arising from the surface friction parameterization (Davies-Jones 2021). Perhaps the free-slip nature of the Guarriello et al. (2018) and Brown and Nowotarski (2019) studies is why they are the only ones known to not contain a premature TLV; however, many other studies featuring a free-slip lower-boundary condition do contain them (Fig. A1). Markowski (2016) also found a strong premature TLV to only occur in a simulation with large crosswise near-surface horizontal vorticity in the background environment; the simulation with large streamwise vorticity did not contain a strong premature TLV. Conversely, the Coffer et al. (2017) and Flournoy et al. (2020) studies—which featured strong premature TLVs—contained a near-surface wind profile largely characterized by streamwise horizontal vorticity (although they did not examine how this profile may have changed in the very-near inflow of the storm). Last, Fischer and Dahl (2022) noted "artificially enhanced" horizontal vorticity around 2–4 km AGL along the periphery of a developing updraft that was initiated using the updraft nudging technique; many parcels originating in subsequent patches of near-surface vertical vorticity maxima originated in this region.

Ultimately, because some recent studies have found barotropic tilting and stretching of background low-level (Markowski 2016; Roberts et al. 2016; Roberts and Xue 2017) and midlevel (Fischer and Dahl 2022) vorticities to strongly influence premature TLV development, we hypothesized that allowing for more gradual updraft development in the simulation would help mitigate this process. As evidenced in this paper, this is at least true for this numerical setup and background homogeneous environment. We are optimistic about the degree to which the tendency nudging technique may help mitigate premature TLV development in other modeling frameworks, but

Study	Time of first vortex (mins)	Initiation	Horizontal radius (km)	Vertical radius (km)	Vertical center (km AGL)	Magnitude	Friction
Roberts et al. (2016)	25	Warm bubble	10	1.5	1.5	6 K	Semi-slip
Roberts and Xue (2017)	25	Warm bubble	10	1.5	1.5	6 K	Semi-slip
Roberts et al. (2020)	25	Warm bubble	10	1.5	1.5	6 K	Semi-slip
Markowski (2016)	15	Heating tendency	3	4.75	5.25	0.07 K s^{-1}	Free-/semi-slip
Fischer and Dahl (2020)	20	Heating tendency	2	0.5	0.7	0.06–0.12 K s^{-1}	Free-slip
Coffer and Parker (2017)	25	Updraft nudging	15	2.5	2.5	15 m s^{-1}	Semi-slip
Coffer and Parker (2018)	50*	Updraft nudging	15	2.5	2.5	15 m s^{-1}	Semi-slip
Coffer et al. (2017)	55*	Updraft nudging	15	2.5	2.5	15 m s^{-1}	Semi-slip
Flournoy et al. (2020)	55*	Updraft nudging	15	2.5	2.5	15 m s^{-1}	Semi-slip
Fischer and Dahl (2022)	45*	Updraft nudging	15	2.5	2.5	15 m s-1	Semi-slip
Dahl et al. (2014)	85	Warm bubble	--	--	--	2 K	Free-slip
Guarriello et al. (2018)	130	Warm bubble	10	1.4	1.4	1 K	Free-slip
Brown and Nowotarski (2019)	130	Warm bubble	10	1.4	1.4	1 K	Free-slip
Boyer and Dahl (2020)	130	Warm bubbles	--	--	--	5 K	Free-slip
Markowski (2020)	40	Warm bubble	10	1.4	1.4	4 K	Semi-slip
Fischer and Dahl (2022)	60	Warm bubble	10	1.4	1.4	5 K	Semi-slip
Markowski and Richardson (2014)	45	Heating tendency	3	4.75	5.25	0.07 K s^{-1}	Free-slip
Markowski and Richardson (2017)	45	Heating tendency	3	4.75	5.25	0.07 K s^{-1}	Free-slip
Rotunno et al. (2017)	40	Heating tendency	3	4.75	5.25	0.07 K s^{-1}	Free-slip
Coffer and Parker (2015)	120	Forced convergence	--	--	--	--	Free-slip
Dahl (2015)	60	Forced convergence	$\lambda_x=\lambda_y = 10^4$	2	0	-10^{-3} s^{-1}	Free-slip
Orf et al. (2017)	60	Updraft nudging	10	1.5	1.5	10 m s^{-1}	Free-slip
Wade and Parker (2021)	85	Updraft nudging	10	1.5	1.5	10 m s^{-1}	Free-slip
This study	175	Tendency nudging	5	1.5	3.5	0.015 K s^{-1}	Semi-slip

FIG. A1. Summary of key characteristics of recent CM1 studies of near-surface vertical vorticity development in supercells. Asterisks in the "time of first vortex" column for some studies indicate that the noted time (as described in their papers) is not representative of the time of an unphysical premature vortex (around t = 20–25 min in each study). The first group of six studies is known to contain premature vortices. In the second group of 12 studies, evidence of premature vortices is less clear. Two of these studies are known to not contain premature vortices (Guarriello et al. 2018; Brown and Nowotarski 2019). The study by Fischer and Dahl (2022) is included twice because they examine a simulation with updraft nudging (which produced a premature vortex) and a warm bubble (which did not). Our study is included at the bottom.

this remains unclear given the uncertainties regarding potential differences in the sources of premature TLV development in different studies.

b. Formulation

The tendency nudging method is derived from the heating tendency approach presented in Markowski and Richardson (2014). The heat source S is defined as

$$S(x, y, z, t) = S_0 R(x, y) Z(z) T(t), \tag{A1}$$

where

$$R(x, y) = \begin{cases} 1 - \dfrac{r^2}{R_w^2} & \text{if } r \le R_w \\ 0 & \text{otherwise} \end{cases}, \tag{A2}$$

$$Z(z) = \begin{cases} 1 - \dfrac{(z - z_w)^2}{Z_w^2} & \text{if } |z - z_w| \le Z_w \\ 0 & \text{otherwise} \end{cases}, \tag{A3}$$

S_0 is the heat source amplitude, R_w is the horizontal radius of the heat source, Z_w is the half-depth of the heat source, $r^2 = (x - x_w)^2 + (y - y_w)^2$, and the heat source is centered at (x_w, y_w, z_w).

The modification to the method of Markowski and Richardson (2014) is the inclusion of a time tendency $T(t)$, defined as

$$T(t) = \begin{cases} \dfrac{t - t_0}{t_1 - t_0} & \text{for } t_0 \le t \le t_1 \\ \dfrac{t_2 - t}{t_2 - t_1} & \text{for } t_1 < t \le t_2 \\ 0 & \text{otherwise} \end{cases}. \tag{A4}$$

In this framework, $T(t)$ increases linearly from 0 to 1 from t_0 to t_1 and decreases linearly back to 0 from t_1 to t_2. This adds a time dependency to the heat source such that it is 0 at the beginning of the desired time period (t_0) and increases to its maximum value (S_0) at $t = t_1$ before returning to 0 at t_2. The values for these parameters are discussed in the main text.

REFERENCES

Bluestein, H. B., and S. S. Parker, 1993: Modes of isolated, severe convective storm formation along the dryline. *Mon. Wea. Rev.*, **121**, 1354–1372, https://doi.org/10.1175/1520-0493(1993)121<1354:MOISCS>2.0.CO;2.

Brown, M., and C. J. Nowotarski, 2019: The influence of lifting condensation level on low-level outflow and rotation in simulated supercell thunderstorms. *J. Atmos. Sci.*, **76**, 1349–1372, https://doi.org/10.1175/JAS-D-18-0216.1.

——, ——, A. R. Dean, B. T. Smith, R. L. Thompson, and J. M. Peters, 2021: The early evening transition in southeastern U.S. tornado environments. *Wea. Forecasting*, **36**, 1431–1452, https://doi.org/10.1175/WAF-D-20-0191.1.

Bryan, G. H., J. C. Wyngaard, and J. M. Fritsch, 2003: Resolution requirements for the simulation of deep moist convection. *Mon. Wea. Rev.*, **131**, 2394–2416, https://doi.org/10.1175/1520-0493(2003)131<2394:RRFTSO>2.0.CO;2.

Buban, M. S., C. L. Ziegler, E. R. Mansell, and Y. P. Richardson, 2012: Simulation of dryline misovortex dynamics and cumulus formation. *Mon. Wea. Rev.*, **140**, 3525–3551, https://doi.org/10.1175/MWR-D-11-00189.1.

Bunkers, M. J., B. A. Klimowski, J. W. Zeitler, R. L. Thompson, and M. L. Weisman, 2000: Predicting supercell motion using a new hodograph technique. *Wea. Forecasting*, **15**, 61–79, https://doi.org/10.1175/1520-0434(2000)015<0061:PSMUAN>2.0.CO;2.

Carbone, R. E., J. W. Conway, N. A. Crook, and M. W. Moncrieff, 1990: The generation and propagation of a nocturnal squall line. Part I: Observations and implications for mesoscale predictability. *Mon. Wea. Rev.*, **118**, 26–49, https://doi.org/10.1175/1520-0493(1990)118<0026:TGAPOA>2.0.CO;2.

——, J. D. Tuttle, D. A. Ahijevych, and S. B. Trier, 2002: Inferences of predictability associated with warm season precipitation episodes. *J. Atmos. Sci.*, **59**, 2033–2056, https://doi.org/10.1175/1520-0469(2002)059<2033:IOPAWW>2.0.CO;2.

Coffer, B. E., and M. D. Parker, 2017: Simulated supercells in nontornadic and tornadic VORTEX2 environments. *Mon. Wea. Rev.*, **145**, 149–180, https://doi.org/10.1175/MWR-D-16-0226.1.

——, and ——, 2018: Is there a "tipping point" between simulated nontornadic and tornadic supercells in VORTEX2 environments? *Mon. Wea. Rev.*, **146**, 2667–2693, https://doi.org/10.1175/MWR-D-18-0050.1.

——, ——, J. M. L. Dahl, L. J. Wicker, and A. J. Clark, 2017: Volatility of tornadogenesis: An ensemble of simulated nontornadic and tornadic supercells in VORTEX2 environments. *Mon. Wea. Rev.*, **145**, 4605–4625, https://doi.org/10.1175/MWR-D-17-0152.1.

Coniglio, M. C., and M. D. Parker, 2020: Insights into supercells and their environments from three decades of targeted radiosonde observations. *Mon. Wea. Rev.*, **148**, 4893–4915, https://doi.org/10.1175/MWR-D-20-0105.1.

Craven, J. P., and H. E. Brooks, 2004: Baseline climatology of sounding derived parameters associated with deep, moist convection. *Natl. Wea. Dig.*, **28**, 13–24.

Dahl, J. M. L., M. D. Parker, and L. J. Wicker, 2014: Imported and storm-generated near-ground vertical vorticity in a simulated supercell. *J. Atmos. Sci.*, **71**, 3027–3051, https://doi.org/10.1175/JAS-D-13-0123.1.

Davenport, C. E., and M. D. Parker, 2015: Impact of environmental heterogeneity on the dynamics of a dissipating supercell thunderstorm. *Mon. Wea. Rev.*, **143**, 4244–4277, https://doi.org/10.1175/MWR-D-15-0072.1.

Davies-Jones, R., 2021: Invented forces in supercell models. *J. Atmos. Sci.*, **78**, 2927–2939, https://doi.org/10.1175/JAS-D-21-0082.1.

Dawson, D. T., II, B. Roberts, and M. Xue, 2019: A method to control the environmental wind profile in idealized simulations of deep convection with surface friction. *Mon. Wea. Rev.*, **147**, 3935–3954, https://doi.org/10.1175/MWR-D-18-0462.1.

Droegemeier, K. K., and R. B. Wilhelmson, 1985: Three-dimensional numerical modeling of convection produced by interacting thunderstorm outflows. Part I: Control simulation and low-level moisture variations. *J. Atmos. Sci.*, **42**, 2381–2403, https://doi.org/10.1175/1520-0469(1985)042<2381:TDNMOC>2.0.CO;2.

Fischer, J., and J. M. L. Dahl, 2020: The relative importance of updraft and cold pool characteristics in supercell tornadogenesis using highly idealized simulations. *J. Atmos. Sci.*, **77**, 4089–4107, https://doi.org/10.1175/JAS-D-20-0126.1.

——, and ——, 2022: Transition of near-ground vorticity dynamics during tornadogenesis. *J. Atmos. Sci.*, **79**, 467–483, https://doi.org/10.1175/JAS-D-21-0181.1.

Flournoy, M. D., M. C. Coniglio, E. N. Rasmussen, J. C. Furtado, and B. E. Coffer, 2020: Modes of storm-scale variability and tornado potential in VORTEX2 near- and far-field tornadic environments. *Mon. Wea. Rev.*, **148**, 4185–4207, https://doi.org/10.1175/MWR-D-20-0147.1.

——, ——, and ——, 2021: Examining relationships between environmental conditions and supercell motion in time. *Wea. Forecasting*, **36**, 737–755, https://doi.org/10.1175/WAF-D-20-0192.1.

——, A. W. Lyza, M. A. Satrio, M. R. Diedrichsen, M. C. Coniglio, and S. Waugh, 2022: A climatology of cell mergers with supercells and their association with mesocyclone evolution. *Mon. Wea. Rev.*, **150**, 451–461, https://doi.org/10.1175/MWR-D-21-0204.1.

Geerts, B., and Coauthors, 2017: The 2015 Plains Elevated Convection at Night field project. *Bull. Amer. Meteor. Soc.*, **98**, 767–786, https://doi.org/10.1175/BAMS-D-15-00257.1.

Gropp, M. E., and C. E. Davenport, 2018: The impact of the nocturnal transition on the lifetime and evolution of supercell thunderstorms in the Great Plains. *Wea. Forecasting*, **33**, 1045–1061, https://doi.org/10.1175/WAF-D-17-0150.1.

Grzych, M. L., B. D. Lee, and C. A. Finley, 2007: Thermodynamic analysis of supercell rear-flank downdrafts from project ANSWERS. *Mon. Wea. Rev.*, **135**, 240–246, https://doi.org/10.1175/MWR3288.1.

Guarriello, F., C. J. Nowotarski, and C. C. Epifanio, 2018: Effects of the low-level wind profile on outflow position and near-surface vertical vorticity in simulated supercell thunderstorms. *J. Atmos. Sci.*, **75**, 731–753, https://doi.org/10.1175/JAS-D-17-0174.1.

Hirth, B. D., J. L. Schroeder, and C. C. Weiss, 2008: Surface analysis of the rear-flank downdraft outflow in two tornadic supercells. *Mon. Wea. Rev.*, **136**, 2344–2363, https://doi.org/10.1175/2007MWR2285.1.

Intrieri, J. M., A. J. Bedard Jr., and R. M. Hardesty, 1990: Details of colliding thunderstorm outflows as observed by Doppler lidar. *J. Atmos. Sci.*, **47**, 1081–1099, https://doi.org/10.1175/1520-0469(1990)047<1081:DOCTOA>2.0.CO;2.

Jorgensen, D. P., and T. M. Weckwerth, 2003: Forcing and organization of convective systems. *Radar and Atmospheric Science: A Collection of Essays in Honor of David Atlas*, *Meteor. Monogr.*, No. 30, Amer. Meteor. Soc., 75–104, https://doi.org/10.1175/0065-9401(2003)030<0075:FAOOCS>2.0.CO;2.

Klees, A. M., Y. P. Richardson, P. M. Markowski, C. Weiss, J. M. Wurman, and K. K. Kosiba, 2016: Comparison of the tornadic and nontornadic supercells intercepted by VORTEX2 on

10 June 2010. *Mon. Wea. Rev.*, **144**, 3201–3231, https://doi.org/10.1175/MWR-D-15-0345.1.

Lasher-Trapp, S., E. Jo, L. R. Allen, B. N. Engelsen, and R. J. Trapp, 2021: Entrainment in a simulated supercell thunderstorm. Part I: The evolution of different entrainment mechanisms and their dilutive effects. *J. Atmos. Sci.*, **78**, 2725–2740, https://doi.org/10.1175/JAS-D-20-0223.1.

Lock, N. A., and A. L. Houston, 2014: Empirical examination of the factors regulating thunderstorm initiation. *Mon. Wea. Rev.*, **142**, 240–258, https://doi.org/10.1175/MWR-D-13-00082.1.

Magee, K. M., and C. E. Davenport, 2020: An observational analysis quantifying the distance of supercell–boundary interactions in the Great Plains. *J. Oper. Meteor.*, **8**, 15–38, https://doi.org/10.15191/nwajom.2020.0802.

Mahoney, W. P., III, 1988: Gust front characteristics and the kinematics associated with interacting thunderstorm outflows. *Mon. Wea. Rev.*, **116**, 1474–1492, https://doi.org/10.1175/1520-0493(1988)116<1474:GFCATK>2.0.CO;2.

Mansell, E. R., 2010: On sedimentation and advection in multimoment bulk microphysics. *J. Atmos. Sci.*, **67**, 3084–3094, https://doi.org/10.1175/2010JAS3341.1.

——, C. L. Ziegler, and E. C. Bruning, 2010: Simulated electrification of a small thunderstorm with two-moment bulk microphysics. *J. Atmos. Sci.*, **67**, 171–194, https://doi.org/10.1175/2009JAS2965.1.

Markowski, P. M., 2016: An idealized numerical simulation investigation of the effects of surface drag on the development of near-surface vertical vorticity in supercell thunderstorms. *J. Atmos. Sci.*, **73**, 4349–4385, https://doi.org/10.1175/JAS-D-16-0150.1.

——, 2020: What is the intrinsic predictability of tornadic supercell thunderstorms? *Mon. Wea. Rev.*, **148**, 3157–3180, https://doi.org/10.1175/MWR-D-20-0076.1.

——, and Y. P. Richardson, 2010: *Mesoscale Meteorology in Midlatitudes*. Wiley-Blackwell, 372 pp.

——, and ——, 2014: The influence of environmental low-level shear and cold pools on tornadogenesis: Insights from idealized simulations. *J. Atmos. Sci.*, **71**, 243–275, https://doi.org/10.1175/JAS-D-13-0159.1.

——, J. M. Straka, E. N. Rasmussen, and D. O. Blanchard, 1998: Variability of storm-relative helicity during VORTEX. *Mon. Wea. Rev.*, **126**, 2959–2971, https://doi.org/10.1175/1520-0493(1998)126<2959:VOSRHD>2.0.CO;2.

——, ——, and ——, 2002: Direct surface thermodynamic observations within the rear-flank downdrafts of nontornadic and tornadic supercells. *Mon. Wea. Rev.*, **130**, 1692–1721, https://doi.org/10.1175/1520-0493(2002)130<1692:DSTOWT>2.0.CO;2.

——, C. Hannon, and E. Rasmussen, 2006: Observations of convection initiation "failure" from the 12 June 2002 IHOP deployment. *Mon. Wea. Rev.*, **134**, 375–405, https://doi.org/10.1175/MWR3059.1.

Naylor, J., and M. S. Gilmore, 2012: Convective initiation in an idealized cloud model using an updraft nudging technique. *Mon. Wea. Rev.*, **140**, 3699–3705, https://doi.org/10.1175/MWR-D-12-00163.1.

Nelson, T. C., J. Marquis, A. Varble, and K. Friedrich, 2021: Radiosonde observations of environments supporting deep moist convection initiation during RELAMPAGO-CACTI. *Mon. Wea. Rev.*, **149**, 289–309, https://doi.org/10.1175/MWR-D-20-0148.1.

Orf, L., R. Wilhelmson, B. Lee, C. Finley, and A. Houston, 2017: Evolution of a long-track violent tornado within a simulated supercell. *Bull. Amer. Meteor. Soc.*, **98**, 45–68, https://doi.org/10.1175/BAMS-D-15-00073.1.

Parker, M. D., 2014: Composite VORTEX2 supercell environments from near-storm soundings. *Mon. Wea. Rev.*, **142**, 508–529, https://doi.org/10.1175/MWR-D-13-00167.1.

Peters, J. M., C. J. Nowotarski, and H. Morrison, 2019: The role of vertical wind shear in modulating maximum supercell updraft velocities. *J. Atmos. Sci.*, **76**, 3169–3189, https://doi.org/10.1175/JAS-D-19-0096.1.

Rasmussen, E. N., and D. O. Blanchard, 1998: A baseline climatology of sounding-derived supercell and tornado forecast parameters. *Wea. Forecasting*, **13**, 1148–1164, https://doi.org/10.1175/1520-0434(1998)013<1148:ABCOSD>2.0.CO;2.

Riganti, C. J., and A. L. Houston, 2017: Rear-flank outflow dynamics and thermodynamics in the 10 June 2010 Last Chance, Colorado, supercell. *Mon. Wea. Rev.*, **145**, 2487–2504, https://doi.org/10.1175/MWR-D-16-0128.1.

Roberts, B., and M. Xue, 2017: The role of surface drag in mesocyclone intensification leading to tornadogenesis within an idealized supercell simulation. *J. Atmos. Sci.*, **74**, 3055–3077, https://doi.org/10.1175/JAS-D-16-0364.1.

——, ——, A. D. Schenkman, and D. T. Dawson II, 2016: The role of surface drag in tornadogenesis within an idealized supercell simulation. *J. Atmos. Sci.*, **73**, 3371–3395, https://doi.org/10.1175/JAS-D-15-0332.1.

——, ——, and D. T. Dawson II, 2020: The effect of surface drag strength on mesocyclone intensification and tornadogenesis in idealized supercell simulations. *J. Atmos. Sci.*, **77**, 1699–1721, https://doi.org/10.1175/JAS-D-19-0109.1.

Rotunno, R., and J. B. Klemp, 1982: The influence of the shear-induced pressure gradient on thunderstorm motion. *Mon. Wea. Rev.*, **110**, 136–151, https://doi.org/10.1175/1520-0493(1982)110<0136:TIOTSI>2.0.CO;2.

——, and J. Klemp, 1985: On the rotation and propagation of simulated supercell thunderstorms. *J. Atmos. Sci.*, **42**, 271–292, https://doi.org/10.1175/1520-0469(1985)042<0271:OTRAPO>2.0.CO;2.

Schueth, A., C. Weiss, and J. M. L. Dahl, 2021: Comparing observations and simulations of the streamwise vorticity current and the forward flank convergence boundary in a supercell storm. *Mon. Wea. Rev.*, **149**, 1651–1671, https://doi.org/10.1175/MWR-D-20-0251.1.

Skinner, P. S., C. C. Weiss, L. J. Wicker, C. K. Potvin, and D. C. Dowell, 2015: Forcing mechanisms for an internal rear-flank downdraft momentum surge in the 18 May 2010 Dumas, Texas, supercell. *Mon. Wea. Rev.*, **143**, 4305–4330, https://doi.org/10.1175/MWR-D-15-0164.1.

Thompson, R. L., R. Edwards, J. A. Hart, K. L. Elmore, and P. Markowski, 2003: Close proximity soundings within supercell environments obtained from the rapid update cycle. *Wea. Forecasting*, **18**, 1243–1261, https://doi.org/10.1175/1520-0434(2003)018<1243:CPSWSE>2.0.CO;2.

Trier, S. B., F. Chen, and K. W. Manning, 2004: A study of convection initiation in a mesoscale model using high-resolution land surface initial conditions. *Mon. Wea. Rev.*, **132**, 2954–2976, https://doi.org/10.1175/MWR2839.1.

Wallace, J. M., 1975: Diurnal variations in precipitation and thunderstorm frequency over the conterminous United States. *Mon. Wea. Rev.*, **103**, 406–419, https://doi.org/10.1175/1520-0493(1975)103<0406:DVIPAT>2.0.CO;2.

Weckwerth, T. M., and D. B. Parsons, 2006: A review of convection initiation and motivation for IHOP_2002. *Mon. Wea. Rev.*, **134**, 5–22, https://doi.org/10.1175/MWR3067.1.

Weisman, M. L., and J. B. Klemp, 1984: The structure and classification of numerically simulated convective storms in directionally varying wind shears. *Mon. Wea. Rev.*, **112**, 2479–2498, https://doi.org/10.1175/1520-0493(1984)112<2479:TSACON>2.0.CO;2.

Wicker, L. J., and R. B. Wilhelmson, 1995: Simulation and analysis of tornado development and decay within a three-dimensional supercell thunderstorm. *J. Atmos. Sci.*, **52**, 2675–2703, https://doi.org/10.1175/1520-0469(1995)052<2675:SAAOTD>2.0.CO;2.

Wilson, J. W., and W. E. Schreiber, 1986: Initiation of convective storms at radar-observed boundary-layer convergence lines. *Mon. Wea. Rev.*, **114**, 2516–2536, https://doi.org/10.1175/1520-0493(1986)114<2516:IOCSAR>2.0.CO;2.

Ziegler, C. L., T. J. Lee, and R. A. Pielke Sr., 1997: Convective initiation at the dryline: A modeling study. *Mon. Wea. Rev.*, **125**, 1001–1026, https://doi.org/10.1175/1520-0493(1997)125<1001:CIATDA>2.0.CO;2.

——, E. N. Rasmussen, M. S. Buban, Y. P. Richardson, L. J. Miller, and R. M. Rabin, 2007: The "triple point" on 24 May 2002 during IHOP. Part II: Ground-radar and in situ boundary layer analysis of cumulus development and convection initiation. *Mon. Wea. Rev.*, **135**, 2443–2472, https://doi.org/10.1175/MWR3411.1.